



Lawrence Berkeley National Laboratory

Earth & Environmental Sciences Area



26 June 2018

Dear Dr. Kala,

My co-authors and I are pleased to submit revised manuscript entitled "*Development and evaluation of a variably saturated flow model in the global E3SM Land Model (ELM) Version 1.0*" for your consideration as a model description paper in *Geoscientific Model Development*.

We thank the executive editor and the two reviewers for their insightful and constructive feedbacks, which helped us clarify important aspects of our work. Modifications made in the revised version of the manuscript as compared to initial submission are summarized below:

1. As suggested by both reviewers, we have highlight the features of VFSM model and justified the increase in 30% computational cost by updating sections 2.2.1, 3.4, and 3.5.
2. The introduction section has been updated to highlight the need for a unified treatment of soil hydrologic processes in unsaturated and saturated zone, which are met by the VFSM developed in this study.
3. The code availability section has been updated to include details about the model version used in the study and the code is now publicly available at <https://github.com/E3SM-Project/E3SM>.
4. Additionally, we have added extensive notes on how to reproduce VFSM benchmarking results against observations and PFLOTRAN at <https://bitbucket.org/gbisht/notes-for-gmd-2018-44>
5. Finally, we have provided detailed response to all comments from the two reviewers.

My co-authors and I believe we have thoroughly addressed all the reviewer comments and that the revised manuscript is well suited for publication in *Geoscientific Model Development*. We look forward to receiving your response.

Sincerely,  
Gautam Bisht

Lawrence Berkeley National Laboratory

One Cyclotron Road / MS: 84-332 / Berkeley, California 94720 / phone 510-486-5036 / [wjriley@lbl.gov](mailto:wjriley@lbl.gov)

1 **Development and evaluation of a variably saturated flow model in the global**  
2 **E3SM Land Model (ELM) Version 1.0**

3

4 **Gautam Bisht<sup>1</sup>, William J. Riley<sup>1</sup>, Glenn E. Hammond<sup>2</sup>, and David M. Lorenzetti<sup>3</sup>**

5

6 <sup>1</sup>Climate & Ecosystem Sciences Division, Lawrence Berkeley National Laboratory,1  
7 Cyclotron Road, Berkeley, California 94720, USA

8

9 <sup>2</sup>Applied Systems Analysis and Research Department, Sandia National Laboratories,  
10 Albuquerque, NM 87185-0747, USA

11

12 <sup>3</sup>Sustainable Energy Systems Group, Lawrence Berkeley National Laboratory,1  
13 Cyclotron Road, Berkeley, California 94720, USA

14

15 Correspondence to: Gautam Bisht (gbisht@lbl.gov)

16 **Abstract**

17 Improving global-scale model representations of coupled surface and groundwater  
18 hydrology is important for accurately simulating terrestrial processes and predicting  
19 climate change effects on water resources. Most existing land surface models,  
20 including the default E3SM Land Model (ELMv0), which we modify here, routinely  
21 employ different formulations for water transport in the vadose and phreatic zones.  
22 In this work, we developed the Variably Saturated Flow Model (VSFM) in ELMv1 to  
23 unify the treatment of soil hydrologic processes in the unsaturated and saturated  
24 zones. VSFM was tested on three benchmark problems and results were evaluated  
25 against observations and an existing benchmark model (PFLOTRAN). The ELMv1-  
26 VSFM's subsurface drainage parameter,  $f_d$ , was calibrated to match an  
27 observationally-constrained and spatially-explicit global water table depth (WTD)  
28 product. Optimal spatially-explicit  $f_d$  values were obtained for 79% of global  $1.9^0 \times$   
29  $2.5^0$  gridcells, while the remaining 21% of global gridcells had predicted WTD deeper  
30 than the observationally-constrained estimate. Comparison with predictions using  
31 the default  $f_d$  value demonstrated that calibration significantly improved predictions,  
32 primarily by allowing much deeper WTDs. Model evaluation using the International  
33 Land Model Benchmarking package (ILAMB) showed that improvements in WTD  
34 predictions did not degrade model skill for any other metrics. We evaluated the  
35 computational performance of the VSFM model and found that the model is about  
36 30% more expensive than the default ELMv0 with an optimal processor layout. The  
37 modular software design of VSFM not only provides flexibility to configure the model  
38 for a range of problem setups, but also allows building the model independently of  
39 the ELM code, thus enabling straightforward testing of model's physics against other  
40 models.

Formatted: Header

Deleted: phreatic

Deleted: An optimal

Deleted: was

Deleted: prediction

## 45 1 Introduction

46 Groundwater, which accounts for 30% of freshwater reserves globally, is a vital  
47 human water resource. It is estimated that groundwater provides 20-30% of global  
48 freshwater withdrawals (Petra, 2009; Zektser and Evertt, 2004), and that irrigation  
49 accounts for ~70% of these withdrawals (Siebert et al., 2010). Climate change is  
50 expected to impact the quality and quantity of groundwater in the future (Alley,  
51 2001). As temporal variability of precipitation and surface water increases in the  
52 future due to climate change, reliance on groundwater as a source of fresh water for  
53 domestic, agriculture, and industrial use is expected to increase (Taylor et al., 2013).

54 Local environmental conditions modulate the impact of rainfall changes on  
55 groundwater resources. For example, high intensity precipitation in humid areas may  
56 lead to a decrease in groundwater recharge (due to higher surface runoff), while arid  
57 regions are expected to see gains in groundwater storage (as infiltrating water  
58 quickly travels deep into the ground before it can be lost to the atmosphere)  
59 (Kundzewicz and Doli, 2009). Although global climate models predict changes in  
60 precipitation over the next century (Marvel et al., 2017), few global models that  
61 participated in the recent Coupled Model Inter-comparison Project (CMIP5; Taylor et  
62 al. (2012)) were able to represent global groundwater dynamics accurately (e.g.  
63 Swenson and Lawrence (2014))

64 Modeling studies have also investigated impacts, at watershed to global [scales](#),  
65 on future groundwater resources associated with land-use (LU) and land-cover (LC)  
66 change (Dams et al., 2008) and ground water pumping (Ferguson and Maxwell, 2012;  
67 Leng et al., 2015). Dams et al. (2008) predicted that LU changes would result in a small  
68 mean decrease in subsurface recharge and large spatial and temporal variability in  
69 groundwater depth for the Kleine Nete basin in Belgium. Ferguson and Maxwell  
70 (2012) concluded that groundwater-fed irrigation impacts on water exchanges with  
71 the atmosphere and groundwater resources can be comparable to those from a 2.5 °C  
72 increase in air temperature for the Little Washita basin in Oklahoma, USA. By  
73 performing global simulations of climate change scenarios using CLM4, Leng et al.  
74 (2015) concluded that the water source (i.e., surface or groundwater) used for

76 irrigation depletes the corresponding water source while increasing the storage of  
77 the other water source. Recently, Leng et al. (2017) showed that irrigation method  
78 (drip, sprinkler, or flood) has impacts on water balances and water use efficiency in  
79 global simulations.

80 Groundwater models are critical for developing understanding of  
81 groundwater systems and predicting impacts of climate (Green et al., 2011). Kollet  
82 and Maxwell (2008) identified critical zones, i.e., regions within the watershed with  
83 water table depths between 1 – 5 m, where the influence of groundwater dynamics  
84 was largest on surface energy budgets. Numerical studies have demonstrated impacts  
85 of groundwater dynamics on several key Earth system processes, including soil  
86 moisture (Chen and Hu, 2004; Liang et al., 2003; Salvucci and Entekhabi, 1995; Yeh  
87 and Eltahir, 2005), runoff generation (Levine and Salvucci, 1999; Maxwell and Miller,  
88 2005; Salvucci and Entekhabi, 1995; Shen et al., 2013), surface energy budgets  
89 (Alkhaier et al., 2012; Niu et al., 2017; Rihani et al., 2010; Soylyu et al., 2011), land-  
90 atmosphere interactions (Anyah et al., 2008; Jiang et al., 2009; Leung et al., 2011;  
91 Yuan et al., 2008), vegetation dynamics (Banks et al., 2011; Chen et al., 2010), and soil  
92 biogeochemistry (Lohse et al., 2009; Pacific et al., 2011).

Deleted: change (Green et al., 2011; Kollet and Maxwell, 2008).

93 Recognizing the importance of groundwater systems on terrestrial processes,  
94 groundwater models of varying complexity have been implemented in land surface  
95 models (LSMs) in recent years. Groundwater models in current LSMs can be classified  
96 into four categories based on their governing equations. Type-1 models assume a  
97 quasi-steady state equilibrium of the soil moisture profile above the water table  
98 (Hilberts et al., 2005; Koster et al., 2000; Walko et al., 2000). Type-2 models use a  $\theta$ -  
99 based (where  $\theta$  is the water volume content) Richards equation in the unsaturated  
100 zone coupled with a lumped unconfined aquifer model in the saturated zone.  
101 Examples of one-dimensional Type-2 models include Liang et al. (2003), Yeh and  
102 Eltahir (2005), Niu et al. (2007), and Zeng and Decker (2009). Examples of quasi  
103 three-dimensional Type-2 models are York et al. (2002); Fan et al. (2007); Miguez-  
104 Macho et al. (2007); and Shen et al. (2013). Type-3 models include a three-  
105 dimensional representation of subsurface flow based on the variably saturated

108 Richards equation (Maxwell and Miller, 2005; Tian et al., 2012). Type-3 models  
109 employ a unified treatment of hydrologic processes in the vadose and ~~phreatic~~ zones  
110 but lump changes associated with water density and unconfined aquifer porosity into  
111 a specific storage term. The fourth class (Type-4) of subsurface flow and reactive  
112 transport models (e.g., PFLOTRAN (Hammond and Lichtner, 2010), TOUGH2 (Pruess  
113 et al., 1999), and STOMP (White and STOMP, 2000)) combine a water equation of  
114 state (EoS) and soil compressibility with the variably saturated Richards equation.  
115 Type-4 models have not been routinely coupled with LSMs to address climate change  
116 relevant research questions. [Clark et al. \(2015\) summarized that most LSMs use  
117 different physics formulations for representing hydrologic processes in saturated and  
118 unsaturated zones. Additionally, Clark et al. \(2015\) identified incorporation of  
119 variably saturated hydrologic flow models \(i.e., Type-3 and Type-4 models\) in LSMs  
120 as a key opportunity for future model development that is expected to improve  
121 simulation of coupled soil moisture and shallow groundwater dynamics.](#)

122 The Energy, Exascale, Earth System Model (E3SM) is a new Earth System  
123 Modeling project sponsored by the U.S. Department of Energy (DOE) ([E3SM Project,  
124 2018](#)). The E3SM model started from the Community Earth System Model (CESM)  
125 version 1\_3\_beta10 (Oleson, 2013). Specifically, the initial version (v0) of the E3SM  
126 Land Model (ELM) was based off the Community Land Model's (CLM's) tag 4\_5\_71.  
127 ELMv0 uses a Type-2 subsurface hydrology model based on Zeng and Decker (2009).  
128 In this work, we developed in ELMv1 a Type-4 Variably Saturated Flow model (VSFM)  
129 to provide a unified treatment of soil hydrologic processes within the unsaturated  
130 and saturated zones. [The VSFM formulation is based on the isothermal, single phase,  
131 variably-saturated \(RICHARDS\) flow model within PFLOTRAN \(Hammond and  
132 Lichtner, 2010\).](#) While PFLOTRAN is a massively parallel, three-dimensional  
133 subsurface model, the VSFM is a serial, one-dimensional model that is appropriate for  
134 climate scale applications.

135 This paper is organized into several sections: (1) brief review of the ELMv0  
136 subsurface hydrology model; (2) overview of the VSFM formulation integrated in  
137 ELMv1; (3) application of the new model formulation to three benchmark problems;  
138 (4) development of a subsurface drainage parameterization necessary to predict

Formatted: Header

Deleted: phreatic

Deleted: ).

Deleted: The VSFM formulation is based on the isothermal single phase flow model of PFLOTRAN (see Hammond and Lichtner (2010) for details regarding various modes supported in PFLOTRAN).

145 global water table depths (WTDs) comparable to recently released observationally-  
 146 constrained estimates; (5) comparison of ELMv1 global simulations with the default  
 147 subsurface hydrology model and VSFM against multiple observations using the  
 148 International Land Model Benchmarking package (ILAMB; Hoffman et al. (2017));  
 149 and (6) a summary of major findings.

## 150 2 Methods

### 151 2.1 Current Model Formulation

152 Water flow in the unsaturated zone is often described by the  $\theta$ -based Richards  
 153 equation:

$$\frac{\partial \theta}{\partial t} = -\nabla \cdot \mathbf{q} - Q \quad (1)$$

154 where  $\theta$  [ $\text{m}^3$  of water  $\text{m}^{-3}$  of soil] is the volumetric soil water content,  $t$  [s] is time,  $\mathbf{q}$   
 155 [ $\text{m s}^{-1}$ ] is the Darcy water flux, and  $Q$  [ $\text{m}^3$  of water  $\text{m}^{-3}$  of soil  $\text{s}^{-1}$ ] is a soil moisture  
 157 sink term. The Darcy flux,  $\vec{q}$ , is given by

$$\mathbf{q} = -K\nabla(\psi + z) \quad (2)$$

158 where  $K$  [ $\text{m s}^{-1}$ ] is the hydraulic conductivity,  $z$  [m] is height above some datum in the  
 159 soil column and  $\psi$  [m] is the soil matric potential. The hydraulic conductivity and soil  
 160 matric potential are modeled as non-linear function of volumetric soil moisture  
 161 following Clapp and Hornberger (1978):

$$K = \theta_{ice} K_{sat} \left( \frac{\theta}{\theta_{sat}} \right)^{2B+3} \quad (3)$$

$$\psi = \psi_{sat} \left( \frac{\theta}{\theta_{sat}} \right)^{-B} \quad (4)$$

162 where  $K_{sat}$  [ $\text{m s}^{-1}$ ] is saturated hydraulic conductivity,  $\psi_{sat}$  [m] is saturated soil  
 163 matric potential,  $B$  is a linear function of percentage clay and organic content (Oleson,  
 164 2013), and  $\theta_{ice}$  is the ice impedance factor (Swenson et al., 2012). ELMv0 uses the

166 modified form of Richards equation of Zeng and Decker (2009) that computes Darcy  
167 flux as

$$\mathbf{q} = -K\nabla(\psi + z - C) \quad (5)$$

168 where C is a constant hydraulic potential above the water table,  $z_v$ , given as

$$C = \psi_E + z = \psi_{sat} \left( \frac{\theta_E(z)}{\theta_{sat}} \right)^{-B} + z = \psi_{sat} + z_v \quad (6)$$

169 where  $\psi_E$  [m] is the equilibrium soil matric potential,  $z$  [m] is height above a  
170 reference datum,  $\theta_E$  [ $\text{m}^3 \text{m}^{-3}$ ] is volumetric soil water content at equilibrium soil  
171 matric potential, and  $z_v$  [m] is height of water table above a reference datum. ELMv0  
172 uses a cell-centered finite volume spatial discretization and backward Euler implicit  
173 time integration. By default, ELMv0's vertical discretization of a soil column yields 15  
174 soil layers of exponentially varying soil thicknesses that reach a depth of 42.1 m Only  
175 the first 10 soils layers (or top 3.8 m of each soil column), are hydrologically active,  
176 while thermal processes are resolved for all 15 soils layers. The nonlinear Darcy flux  
177 is linearized using Taylor series expansion and the resulting tridiagonal system of  
178 equations is solved by LU factorization.

179 Flow in the saturated zone is modeled as an unconfined aquifer below the soil  
180 column based on the work of Niu et al. (2007). Exchange of water between the soil  
181 column and unconfined aquifer depends on the location of the water table. When the  
182 water table is below the last hydrologically active soil layer in the column, a recharge  
183 flux from the last soil layer replenishes the unconfined aquifer. A zero-flux boundary  
184 condition is applied to the last hydrologically active soil layer when the water table is  
185 within the soil column. The unconfined aquifer is drained by a flux computed based  
186 on the SIMTOP scheme of Niu et al. (2007) with modifications to account for frozen  
187 soils (Oleson, 2013).

## 188 2.2 New VSFM Model Formulation

189 In the VSFM formulation integrated in ELMv1, we use the mass conservative form of  
190 the variably saturated subsurface flow equation (Farthing et al., 2003; Hammond and  
191 Lichtner, 2010; Kees and Miller, 2002):

Formatted: Header

Deleted: =  $\psi_{sat}$

Formatted: Font color: Auto

Deleted: the



Formatted: Header

$$\frac{\partial(\phi s_w \rho)}{\partial t} = -\nabla \cdot (\rho \mathbf{q}) - Q \quad (7)$$

194 where  $\phi$  [m<sup>3</sup> m<sup>-3</sup>] is the soil porosity,  $s_w$  [-] is saturation,  $\rho$  [kg m<sup>-3</sup>] is water density,  
195  $\mathbf{q}$  [m s<sup>-1</sup>] is the Darcy velocity, and  $Q$  [kg m<sup>-3</sup> s<sup>-1</sup>] is a water sink. We restrict our model  
196 formulation to a one-dimensional system and the flow velocity is defined by Darcy's  
197 law:

$$\mathbf{q} = -\frac{kk_r}{\mu} \nabla(P + \rho g z) \quad (8)$$

198 where  $k$  [m<sup>2</sup>] is intrinsic permeability,  $k_r$  [-] is relative permeability,  $\mu$  [Pa s] is  
199 viscosity of water,  $P$  [Pa] is pressure,  $g$  [m s<sup>-2</sup>] is the acceleration due to gravity, and  
200  $z$  [m] is elevation above some datum in the soil column.

201 In order to close the system, a constitutive relationship is used to express  
202 saturation and relative permeability as a function of soil matric pressure. Analytic  
203 Water Retention Curves (WRCs) are used to model effective saturation ( $s_e$ )

$$s_e = \left( \frac{s_w - s_r}{1 - s_r} \right) \quad (9)$$

204 where  $s_w$  is saturation and  $s_r$  is residual saturation. We have implemented Brooks  
205 and Corey (1964) (equation 10) and van Genuchten (1980) (equation 11) WRCs:

$$s_e = \begin{cases} \left( \frac{-P_c}{P_c^0} \right)^{-\lambda} & \text{if } P_c < 0 \\ 1 & \text{if } P_c \geq 0 \end{cases} \quad (10)$$

$$s_e = \begin{cases} [1 + (\alpha |P_c|)^n]^{-m} & \text{if } P_c < 0 \\ 1 & \text{if } P_c \geq 0 \end{cases} \quad (11)$$

206 where  $P_c$  [Pa] is the capillary pressure,  $P_c^0$  [Pa] is the air entry pressure, and  $\alpha$  [Pa<sup>-1</sup>]  
207 is inverse of the air entry pressure. The capillary pressure is computed as  $P_c = P -$   
208  $P_{ref}$  where  $P_{ref}$  is  $P_c^0$  for Brooks and Corey WRC and typically the atmospheric  
209 pressure (=101,325 [Pa]) is used for van Genuchten WRC. In addition, a smooth  
210 approximation of equation (10) and (11) was developed to facilitate convergence of  
211 the nonlinear solver (Appendix A). Relative soil permeability was modeled using the  
212 Mualem (1976) formulation:

Deleted: ,

Deleted: soil

Deleted: soil

Deleted: soil

Deleted: and

Deleted: capillary pressure denoting

Deleted: point

$$\kappa_r(s_e) = \begin{cases} s_e^{0.5} \left[ 1 - \left( 1 - s_e^{1/m} \right)^m \right] & \text{if } P < P_{ref} \\ 1 & \text{if } P \geq P_{ref} \end{cases} \quad (12)$$

220 Lastly, we used an EoS for water [density,  \$\rho\$ , that is a nonlinear function of liquid](#)  
 221 [pressure,  \$P\$ , and liquid temperature,  \$T\$](#) , given by Tanaka et al. (2001):

$$\rho(P, T) = [1 + (k_0 + k_1T + k_2T^2)(P - P_{ref})]a_5 \left[ 1 - \frac{(T + a_1)^2(T + a_2)}{a_3(T + a_4)} \right] \quad (13)$$

222 where

$$\begin{aligned} k_0 &= 50.74 \times 10^{-11} \text{ [Pa}^{-1}\text{]} \\ k_1 &= -0.326 \times 10^{-11} \text{ [Pa}^{-1}\text{C}^{-1}\text{]} \\ k_2 &= 0.00416 \times 10^{-11} \text{ [Pa}^{-1}\text{C}^2\text{]} \\ a_1 &= -3.983035 \text{ [C]} \\ a_2 &= 301.797 \text{ [C]} \\ a_3 &= 522558.9 \text{ [C}^{-2}\text{]} \\ a_4 &= 69.34881 \text{ [C]} \\ a_5 &= 999.974950 \text{ [kg m}^{-3}\text{]} \end{aligned}$$

223 Unlike the default subsurface hydrology model, the VSFM is applied over the  
 224 full soil depth (in the default model, 15 soil layers). The VSFM model replaces both  
 225 the  $\theta$ -based Richards equation and the unconfined aquifer of the default model [and](#)  
 226 [uses a zero-flux lower boundary condition](#). In the VSFM model, water table depth is  
 227 diagnosed based on the vertical soil liquid pressure profile. Like the default model,  
 228 drainage flux is computed based on the modified SIMTOP approach and is vertically  
 229 distributed over the soil layers below the water table.

### 230 2.2.1 Discrete Equations

231 We use a cell-centered finite volume discretization to decompose the spatial  
 232 domain,  $\Omega$ , into  $N$  non-overlapping control volumes,  $\Omega_n$ , such that  $\Omega = \cup_{n=1}^N \Omega_n$  and  $\Gamma_n$   
 233 represents the boundary of the  $n$ -th control volume. Applying a finite volume integral  
 234 to equation (7) and the divergence theorem yields

$$\frac{\partial}{\partial t} \int_{\Omega_n} (\phi s_w \rho) dV = - \int_{\Gamma_n} (\rho \mathbf{q}) \cdot d\mathbf{A} - \int_{\Omega_n} Q dV \quad (14)$$

Formatted: Header

Formatted: Font color: Auto

Deleted: .

236 The discretized form of the left hand side term and first term on the right hand side  
 237 of equation (14) are approximated as:  
 238

$$\frac{\partial}{\partial t} \int_{\Omega_n} (\phi s_w \rho) dV \approx \left( \frac{d}{dt} (\phi s_w \rho) \right) V_n \quad (15)$$

$$\int_{\Gamma_n} (\rho \mathbf{q}) \cdot d\mathbf{A} \approx \sum_{n'} (\rho \mathbf{q})_{nn'} \cdot \mathbf{A}_{nn'} \quad (16)$$

239 After substituting equations (15) and (16) in equation (14), the resulting ordinary  
 240 differential equation for the variably saturated flow model is

$$\left( \frac{d}{dt} (\phi s_w \rho) \right) V_n = - \sum_{n'} (\rho \mathbf{q})_{nn'} \cdot \mathbf{A}_{nn'} - Q_n V_n \quad (17)$$

241 We perform temporal integration of equation (17) using the backward-Euler scheme:

$$\left( \frac{(\phi s_w \rho)_n^{t+1} - (\phi s_w \rho)_n^t}{\Delta t} \right) V_n = - \sum_{n'} (\rho \mathbf{q})_{nn'}^{t+1} \cdot \mathbf{A}_{nn'} - Q_n^{t+1} V_n \quad (18)$$

242 Rearranging terms of equation (18) results in a nonlinear equation for the unknown  
 243 pressure at timestep  $t + 1$  as

$$\left( \frac{(\phi s_w \rho)_n^{t+1} - (\phi s_w \rho)_n^t}{\Delta t} \right) V_n + \sum_{n'} (\rho \mathbf{q})_{nn'}^{t+1} \cdot \mathbf{A}_{nn'} + Q_n^{t+1} V_n = 0 \quad (19)$$

244 In this work, we find the solution to the [nonlinear](#) system of nonlinear equations given  
 245 by equation (19) using Newton's method [via the Scalable Nonlinear Equations Solver](#)  
 246 [\(SNES\) within](#) the Portable, Extensible Toolkit for Scientific Computing (PETSc)  
 247 library (Balay et al., 2016). PETSc provides a suite of data structures and routines for  
 248 the scalable solution of partial differential equations. [VSFM uses the composable data](#)  
 249 [management \(DMComposite\) provided by PETSc \(Brown et al., 2012\), which enables](#)  
 250 [the potential future application of the model to solve tightly coupled multi-](#)  
 251 [component, multi-physics processes as discussed in section 3.4.](#) A Smooth  
 252 approximation of the Brooks and Corey (1964) (SBC) water retention curve was  
 253 developed to facilitate faster convergence of the nonlinear solver (Appendix A).  
 254 [ELMv0 code for subsurface hydrologic processes only supports two vertical mesh](#)

256 [configurations and a single set of boundary and source-sink conditions. Moreover, the](#)  
257 [monolithic ELMv0 code does not allow for testing of individual process](#)  
258 [representations against analytical solutions or simulation results from other models.](#)  
259 [The modular software design of VSFM overcomes ELMv0's software limitation by](#)  
260 [allowing VSFM code to be built independently of the ELM code. This flexibility of](#)  
261 [VSFM's build system allows for testing of the VSFM physics in isolation without any](#)  
262 [influence from the rest of ELM's physics formulations. Additionally, VSFM can be](#)  
263 [easily configured for a wide range of benchmark problems with different spatial grid](#)  
264 [resolutions, material properties, boundary conditions, and source-sink forcings.](#)

### 265 2.3 VSFM single-column evaluation

266 We tested the VSFM with three idealized 1-dimensional test problems. First, the  
267 widely studied problem for 1D Richards equation of infiltration in dry soil by Celia et  
268 al. (1990) was used. The problem setup consists of a 1.0 m long soil column with a  
269 uniform initial pressure of  $-10.0$  m (= 3535.5 Pa). Time invariant boundary  
270 conditions applied at the top and bottom of soil column are  $-0.75$  m (= [93989.1](#) Pa)  
271 and  $-10.0$  m (= 3535.5 Pa), respectively. The soil properties for this test are given in  
272 Table 1. A vertical discretization of 0.01 m is used in this simulation.

273 Second, we simulated transient one-dimensional vertical infiltration in [a](#) two-  
274 layered soil system as described in Srivastava and Yeh (1991). The domain consisted  
275 of a 2 m tall soil column divided equally in two soil types. Except [for](#) soil [intrinsic](#)  
276 permeability, all other soil properties of the two soil types are the same. The bottom  
277 soil is 10 times less permeable than the top (Table1). Unlike Srivastava and Yeh  
278 (1991), who used exponential functions of soil liquid pressure to compute hydraulic  
279 conductivity and soil saturation, we used Mualem (1976) and van Genuchten (1980)  
280 constitutive relationships. Since our choice of constitutive relationships for this setup  
281 resulted in absence of an analytical solution, we compared VSFM simulations against  
282 PFLOTRAN results. The domain was discretized in 200 control volumes of equal soil  
283 thickness. Two scenarios, wetting and drying, were modeled to test the robustness of  
284 the VSFM solver robustness. Initial conditions for each scenario included a time  
285 invariant boundary condition of 0 m (=  $1.01325 \times 10^5$  Pa) for the lowest control

287 volume and a constant flux of  $0.9 \text{ cm hr}^{-1}$  and  $0.1 \text{ cm hr}^{-1}$  at the soil surface for wetting  
 288 and drying scenarios, respectively.

289 Third, we compare VFSM and PFLOTRAN predictions for soil under variably  
 290 saturated conditions. The 1-dimensional 1 m deep soil column was discretized in 100  
 291 equal thickness control volumes. A hydrostatic initial condition was applied such that  
 292 water table is 0.5 m below the soil surface. A time invariant flux of  $2.5 \times 10^{-5} \text{ m s}^{-1}$  is  
 293 applied at the surface, while the lowest control volume has a boundary condition  
 294 corresponding to the initial pressure value at the lowest soil layer. The soil properties  
 295 used in this test are the same as those used in the first evaluation.

#### 296 **2.4 Global Simulations and groundwater depth analysis**

297 We performed global simulations with ELMv1-VFSM at a spatial resolution of  
 298  $1.9^{\circ}$  (latitude)  $\times$   $2.5^{\circ}$  (longitude) with a 30 [min] time-step for 200 years, including a  
 299 180 year spinup and the last 20 years for analysis. The simulations were driven by  
 300 CRUNCEP meteorological forcing from 1991-2010 (Piao et al., 2012) and configured  
 301 to use prescribed satellite phenology.

302 For evaluation and calibration, we used the Fan et al. (2013) global  $\sim 1 \text{ km}$   
 303 horizontal resolution WTD dataset (hereafter F2013 dataset), which is based on a  
 304 combination of observations and hydrologic modeling. We aggregated the dataset to  
 305 the ELMv1-VFSM spatial resolution. ELM-VFSM's default vertical soil discretization  
 306 uses 15 soil layers to a depth of  $\sim 42 \text{ m}$ , with an exponentially varying soil thickness.  
 307 However,  $\sim 13\%$  of F2013 land gridcells have a water table deeper than 42 m. We  
 308 therefore modified ELMv1-VFSM to extend the soil column to a depth of 150 m with  
 309 59 soil layers; the first nine soil layer thicknesses were the same as described in  
 310 Oleson (2013) and the remaining layers (10-59) were set to a thickness of 3 m.

#### 311 **2.5 Estimation of the subsurface drainage parameterization**

312 In the VFSM formulation, the dominant control on long-term GW depth is the  
 313 subsurface drainage flux,  $q_d$  [ $\text{kg m}^{-2} \text{ s}^{-1}$ ], which is calculated based on water table  
 314 depth,  $z_v$  [m], (Niu et al. (2005)):

$$q_d = q_{d,max} \exp(-f_d z_v) \quad (20)$$

Formatted: Header

315 where  $q_{d,max}$  [ $\text{kg m}^{-2} \text{s}^{-1}$ ] is the maximum drainage flux that depends on gridcell slope  
316 and  $f_d$  [ $\text{m}^{-1}$ ] is an empirically-derived parameter. The subsurface drainage flux  
317 formulation of Niu et al. (2005) is similar to the TOPMODEL formulation (Beven and  
318 Kirkby, 1979) and assumes the water table is parallel to the soil surface. While  
319 Sivapalan et al. (1987) derived  $q_{d,max}$  as a function of lateral hydraulic anisotropy,  
320 hydraulic conductivity, topographic index, and decay factor controlling vertical  
321 saturated hydraulic conductivity, Niu et al. (2005) defined  $q_{d,max}$  as a single  
322 calibration parameter. ELMv0 uses  $f_d = 2.5 \text{ m}^{-1}$  as a global constant and estimates  
323 maximum drainage flux when WTD is at the surface as  $q_{d,max} = 10 \sin(\beta) \text{ kg m}^{-2} \text{ s}^{-1}$ .  
324 <sup>1</sup>. Of the two parameters,  $f_d$  and  $q_{d,max}$ , available for model calibration, we choose to  
325 calibrate  $f_d$  because the uncertainty analysis by Hou et al. (2012) identified it as the  
326 most significant hydrologic parameter in CLM4. To improve on the  $f_d$  parameter  
327 values, we performed an ensemble of global simulations with  $f_d$  values of 0.1, 0.2, 0.5,  
328 1.0, 2.5, 5.0, 10.0, and 20  $\text{m}^{-1}$ . Each ensemble simulation was run for 200 years to  
329 ensure an equilibrium solution, and the last 20 years were used for analysis. A non-  
330 linear functional relationship between  $f_d$  and  $WTD$  was developed for each gridcell  
331 and then the F2013 dataset was used to estimate an optimal  $f_d$  for each gridcell.

Deleted:  $\sin(\beta)$

## 332 2.6 Global ELM-VSFM evaluation

333 With the optimal  $f_d$  values, we ran a ELM-VSFM simulation using the protocol  
334 described above. We then used the International Land Model Benchmarking package  
335 (ILAMB) to evaluate the ELMv1-VSFM predictions of surface energy budget, total  
336 water storage anomalies (TWSA), and river discharge (Collier et al., 2018; Hoffman et  
337 al., 2017). ILAMB evaluates model prediction bias, RMSE, and seasonal and diurnal  
338 phasing against multiple observations of energy, water, and carbon cycles at in-situ,  
339 regional, and global scales. Since ELM-VSFM simulations in this study did not include  
340 an active carbon cycle, we used the following ILAMB benchmarks for water and  
341 energy cycles: (i) latent and surface energy fluxes using site-level measurements from  
342 FLUXNET (Lasslop et al., 2010) and globally from FLUXNET-MTE (Jung et al., 2009));  
343 (ii) terrestrial water storage anomaly (TWSA) from the Gravity Recovery And Climate  
344 Experiment (GRACE) observations (Kim et al., 2009); and (iii) stream flow for the 50

Deleted: .

347 largest global river basins (Dai and Trenberth, 2002). We applied ILAMB benchmarks  
348 for ELMv1-VSFM simulations with default and calibrated  $f_d$  to ensure improvements  
349 in WTD predictions did not degrade model skill for other processes.

### 350 **3 Results and discussion**

#### 351 **3.1 VSFM single-column evaluation**

352 For the 1D Richards equation infiltration in dry soil comparison, we evaluated  
353 the solutions at 24-hr against those published by Celia et al. (1990) (Figure 1). The  
354 VSFM solver accurately represented the sharp wetting front over time, where soil  
355 hydraulic properties change dramatically due to non-linearity in the soil water  
356 retention curve.

357 For the model evaluation of infiltration and drying in layered soil, the results of  
358 the VSFM and PFLOTRAN are essentially identical. In both models and scenarios, the  
359 higher permeability top soil responds rapidly to changes in the top boundary  
360 condition and the wetting and drying fronts progressively travel through the less  
361 permeable soil layer until soil liquid pressure in the entire column reaches a new  
362 steady state by about 100 h (Figure 2).

363 We also evaluated the VSFM predicted water table dynamics against PFLOTRAN  
364 predictions from an initial condition of saturated soil below 0.5 m depth. The  
365 simulated water table rises to 0.3 m depth by 1 day and reaches the surface by 2 days,  
366 and the VSFM and PFLOTRAN predictions are essentially identical Figure 3. These  
367 three evaluation simulations demonstrate the VSFM accurately represents soil  
368 moisture dynamics under conditions relevant to ESM-scale prediction.

#### 369 **3.2 Subsurface drainage parameterization estimation**

370 The simulated nonlinear WTD- $f_d$  relationship is a result of the subsurface  
371 drainage parameterization flux given by equation (20) (Figure 4(a) and (b)). For  
372  $0.1 \leq f_d \leq 1$ , the slope of the WTD- $f_d$  relationship for all gridcells is log-log linear  
373 with a slope of  $-1.0 \pm 0.1$ . The log-log linear relationship breaks down for  $f_d > 1$ ,  
374 where the drainage flux becomes much smaller than infiltration and

375 evapotranspiration (Figure 4(c) and (d)). Thus, at larger  $f_d$ , the steady state  $z_v$   
376 becomes independent of  $f_d$  and is determined by the balance of infiltration and  
377 evapotranspiration.

378 For 79% of the global gridcells, the ensemble range of simulated WTD spanned  
379 the F2013 dataset. The optimal value of  $f_d$  for each of these gridcells was obtained by  
380 linear interpolation in the log-log space (e.g., Figure 4 (a)). For the remaining 21% of  
381 gridcells where the shallowest simulated WTD across the range of  $f_d$  was deeper than  
382 that in the F2013 dataset, the optimal  $f_d$  value was chosen as the one that resulted in  
383 the lowest absolute WTD error (e.g., Figure 4 (b)). At large  $f_d$  values, the drainage flux  
384 has negligible effects on WTD, yet simulated WTD is not sufficiently shallow to match  
385 the F2013 observations, which indicates that either evapotranspiration is too large  
386 or infiltration is too small. There was no difference in the mean percentage of sand  
387 and clay content between grids cells with and without an optimal  $f_d$  value. The  
388 optimal  $f_d$  has a global average of  $1.60 \text{ m}^{-1} \pm 2.68 \text{ m}^{-1}$  and 72% of global gridcells have  
389 an optimal  $f_d$  value lower than the global average (Figure 5).

### 390 3.3 Global simulation evaluation

391 The ELMv1-VSFM predictions are much closer to the F2013 dataset (Figure 6a)  
392 using optimal globally-distributed  $f_d$  values (Figure 6c) compared to the default  $f_d$   
393 value (Figure 6b). The significant reduction in WTD bias (model - observation) is  
394 mostly due to improvement in the model's ability to accurately predict deep WTD  
395 using optimal  $f_d$  values. In the simulation using optimal globally-distributed  $f_d$   
396 values, all gridcells with WTD bias > 3.7 m were those for which an optimal  $f_d$  was  
397 not found. The mean global bias, RMSE, and  $R^2$  values improved in the new ELMv1-  
398 VSFM compared to the default model (Table 1). The 79% of global grid cells for which  
399 an optimal  $f_d$  value was estimated had significantly better water table prediction  
400 with a bias, RMSE, and  $R^2$  of -0.04 m, 0.67 m, and 0.99, respectively, as compared to  
401 the remaining 21% of global gridcells that had a bias, RMSE, and  $R^2$  of -9.82 m, 18.08  
402 m, and 0.31, respectively. The simulated annual WTD range, which we define to be  
403 the difference between maximum and minimum WTD in a year, has a spatial mean  
404 and standard deviation of 0.32 m and 0.58 m, respectively, using optimal  $f_d$  values

Formatted: Header

Deleted: effect

Deleted: were all

Deleted: Table 1

Deleted: 67m

Deleted: grid

Deleted: 08m



411 (Figure 7 (a)). The annual WTD range decreased by 0.24 m for the 79% of the grid  
 412 cells for which an optimal  $f_d$  value was estimated (Figure 7 (b)).

413 Globally-averaged WTD in ELMv1-VSFM simulations with default  $f_d$  and  
 414 optimal  $f_d$  values were 10.5 m and 20.1 m, respectively. Accurate prediction of deep  
 415 WTD in the simulation with optimal  $f_d$  caused very small differences in near-surface  
 416 soil moisture (Figure 8). The 79% of grid cells with an optimal  $f_d$  value had deeper  
 417 globally-averaged WTDs than when using the default  $f_d$  value (24.3 m vs. 8.6 m). For  
 418 these 79% of grid cells, the WTD was originally deep enough to not impact near-  
 419 surface conditions (Kollet and Maxwell, 2008); therefore, further lowering of WTD  
 420 led to negligible changes in near-surface hydrological conditions.

421 The International Land Model Benchmarking (ILAMB) package (Hoffman et al.,  
 422 2017) provides a comprehensive evaluation of predictions of carbon cycle states and  
 423 fluxes, hydrology, surface energy budgets, and functional relationships by  
 424 comparison to a wide range of observations. We used ILAMB to evaluate the  
 425 hydrologic and surface energy budget predictions from the new ELMv1-VSFM model  
 426 (Table 3). Optimal  $f_d$  values had inconsequential impacts on simulated surface  
 427 energy fluxes at site-level and global scales. Optimal  $f_d$  values led to improvement in  
 428 prediction of deep WTD (with a mean value of 24.3 m) for grid cells that had an  
 429 average WTD of 8.7 m in the simulation using default  $f_d$  values. Thus, negligible  
 430 differences in surface energy fluxes between the two simulations are consistent with  
 431 the findings of Kollet and Maxwell (2008), who identified decoupling of groundwater  
 432 dynamics and surface processes at a WTD of  $\sim 10$  m. There were slight changes in bias  
 433 and RMSE for predicted TWSA, but the ILAMB score remained unchanged. The TWSA  
 434 amplitude is lower for the simulation with optimal  $f_d$  values, consistent with the  
 435 associated decrease in annual WTD range. ELM's skill in simulating runoff for the 50  
 436 largest global watersheds remained unchanged.

437 Finally, we evaluated the computational costs of implementing VSFM in ELM  
 438 [and compared them to the default model. We performed 5-year long simulations for](#)  
 439 [default and VSFM using 96, 192, 384, 768, and 1536 cores on the Edison](#)  
 440 [supercomputer at the National Energy Research Scientific Computing Center. Using](#)  
 441 [an optimal processor layout, we found that ELMv1-VSFM is  \$\sim 30\%\$  more expensive](#)

Formatted: Normal1

**Deleted:** , and compared them to the default model. We performed 5-years long simulations for default and VSFM using 96, 192, 384, 768, and 1536 cores on the Edison supercomputer at the National Energy Research Scientific Computing Center. Using an optimal processor layout, we found that ELMv1-VSFM is  $\sim 30\%$  more expensive than the default ELMv1 model

|

449 [than the default ELMv1 model. We note that the relative computational cost of the](#)  
450 [land model in a fully coupled global model simulation is generally very low. Dennis et](#)  
451 [al. \(2012\) reported computational cost of the land model to be less than 1% in ultra-](#)  
452 [high-resolution CESM simulations. We therefore believe that the additional benefits](#)  
453 [associated with the VSFM formulation are well justified by this modest increase in](#)  
454 [computational cost. In particular, VSFM allows a greater variety of mesh](#)  
455 [configurations and boundary conditions, and can accurately simulate WTD for the](#)  
456 [~13% of global grid cells that have a water table deeper than 42 \[m\] \(Fan et al. \(2013\),](#)

### 457 **3.4 Caveats and Future Work**

458 The significant improvement in WTD prediction using optimal  $f_d$  values  
459 demonstrates VSFM's capabilities to model hydrologic processes using a unified  
460 physics formulation for unsaturated-saturated zones. However, several caveats  
461 remain due to uncertainties in model structure, model parameterizations, and climate  
462 forcing data.

463 In this study, we assumed a spatially homogeneous depth to bedrock (DTB) of  
464 150 m. Recently, Brunke et al. (2016) incorporated a global ~1 km dataset of soil  
465 thickness and sedimentary deposits (Pelletier et al., 2016) in CLM4.5 to study the  
466 impacts of soil thickness spatial heterogeneity on simulated hydrological and thermal  
467 processes. While inclusion of heterogeneous DTB in CLM4.5 added more realism to  
468 the simulation setup, no significant changes in simulated hydrologic and energy  
469 fluxes were reported by Brunke et al. (2016). Presently, work is ongoing in the E3SM  
470 project to include variable DTB within ELM and future simulations will examine the  
471 impact of those changes on VSFM's prediction of WTD. Our use of the 'satellite  
472 phenology' mode, which prescribes transient LAI profiles for each plant functional  
473 type in the gridcell, ignored the likely influence of water cycle dynamics and nutrient  
474 constraints on the C cycle (Ghimire et al., 2016; Zhu et al., 2016). [Estimation of soil](#)  
475 [hydraulic properties based on soil texture data is critical for accurate LSM predictions](#)  
476 [\(Gutmann and Small, 2005\) and this study does not account for uncertainty in soil](#)  
477 [hydraulic properties.](#)

Formatted: Header

Formatted: Font color: Black

Formatted: Font color: Accent 1

Formatted: Left

478 Lateral water redistribution impacts soil moisture dynamics (Bernhardt et al.,  
479 2012), biogeochemical processes in the root zone (Grant et al., 2015), distribution of  
480 vegetation structure (Hwang et al., 2012), and land-atmosphere interactions (Chen  
481 and Kumar, 2001; Rihani et al., 2010). The ELMv1-VSFM developed in this study does  
482 not include lateral water redistribution between soil columns and only simulates  
483 vertical water transport. Lateral subsurface processes can be included in LSMs via a  
484 range of numerical discretization approaches of varying complexity, e.g., adding  
485 lateral water as source/sink terms in the 1D model, implementing an operator split  
486 approach to solve vertical and lateral processes in a non-iterative approach (Ji et al.,  
487 2017), or solving a fully coupled 3D model (Bisht et al., 2017; Bisht et al., 2018; Kollet  
488 and Maxwell, 2008). Additionally, lateral transport of water can be implemented in  
489 LSMs at a subgrid level (Milly et al., 2014) or grid cell level (Miguez-Macho et al.,  
490 2007). The current implementation of VSFM is such that each processor solves the  
491 variably saturated Richards equation for all independent soil columns as one single  
492 problem. Thus, extension of VSFM to solve the tightly coupled 3D Richards equation  
493 on each processor locally while accounting for lateral transport of water within grid  
494 cells and among grid cells is straightforward. The current VSFM implementation can  
495 also be easily extended to account for subsurface transport of water among grid cells  
496 that are distributed across multiple processors by modeling lateral flow as  
497 source/sink terms in the 1D model. Tradeoffs between approaches to represent  
498 lateral processes and computational costs need to be carefully studied before  
499 developing quasi or fully three-dimensional land surface models (Clark et al., 2015).  
500 Transport of water across multiple components of the Soil Plant Atmosphere  
501 Continuum (SPAC) has been identified as a critical process in understanding the  
502 impact of climate warming on the global carbon cycle (McDowell and Allen, 2015).  
503 Several SPAC models have been developed by the ecohydrology community and  
504 applied to study site-level processes (Amenu and Kumar, 2008; Bohrer et al., 2005;  
505 Manoli et al., 2014; Sperry et al., 1998), yet implementation of SPAC models in global  
506 LSMs is limited (Clark et al., 2015). Similarly, current generation LSMs routinely  
507 ignore advective heat transport within the subsurface, which has been shown to be  
508 important in high-latitude environments by multiple field and modeling studies

Formatted: Header

Deleted: VSFM

Deleted: a

Deleted: .

|

Formatted: Header

512 [\(Bense et al., 2012; Frampton et al., 2011; Grant et al., 2017; Kane et al., 2001\)](#). The  
513 [use of PETSc's DMComposite in VSFM provides flexibility for solving a tightly coupled](#)  
514 [multi-component problem \(e.g., transport of water through the soil-plant continuum\)](#)  
515 [and multi-physics problem \(e.g., fully coupled conservation of mass and energy](#)  
516 [equations in the subsurface\)](#). [DMComposite allows for an easy assembly of a tightly](#)  
517 [coupled multi-physics problem from individual physics formulations \(Brown et al.,](#)  
518 [2012\)](#).

#### 519 4 Summary and Conclusion

520 Starting from the climate-scale land model ELMv0, we incorporated a unified  
521 physics formulation to represent soil moisture and groundwater dynamics that are  
522 solved using PETSc. Application of VSFM to three benchmarks problems  
523 demonstrated its robustness to simulated subsurface hydrologic processes in  
524 coupled unsaturated and saturated zones. Ensemble global simulations at  $1.9^0 \times 2.5^0$   
525 were performed for 200 years to obtain spatially heterogeneous [estimates](#) of [the](#)  
526 subsurface drainage parameter,  $f_d$ , that minimized [mismatches](#) between predicted  
527 and observed [WTDs](#). In order to [simulate](#) the deepest water table reported in the Fan  
528 et al. (2013) dataset, we used 59 vertical soil layers that reached a depth of 150 m.

Deleted: estimate

Deleted: a

Deleted: the mismatch

Deleted: WTD

Deleted: simulated

529 An optimal  $f_d$  was obtained for 79% of the grids cells in the domain. For the  
530 remaining 21% of grid cells, simulated WTD always remained deeper than observed.  
531 Calibration of  $f_d$  significantly improved global WTD prediction by reducing bias and  
532 RMSE and increasing  $R^2$ . Grids without an optimal  $f_d$  were the largest contributor of  
533 error in WTD prediction. ILAMB benchmarks on simulations with default and  
534 optimal  $f_d$  showed negligible changes to surface energy fluxes, TWSA, and runoff.  
535 [ILAMB](#) metrics ensured that model skill was not adversely impacted for all other  
536 processes when optimal  $f_d$  values were used to improve WTD prediction.

Deleted: ILAMB

537

544 **5 Appendix**

545 **5.1 Smooth approximation of Brooks-Corey water retention curve**

546 The Brooks and Corey (1964) water retention curve of equation (10) has a  
 547 discontinuous derivative at  $P = P_c^0$ . Figure A 1 [illustrates](#) an example. To improve  
 548 convergence of the nonlinear solver at small capillary pressures, the smoothed  
 549 Brooks-Corey function introduces a cubic polynomial,  $B(P_c)$ , in the neighborhood of  
 550  $P_c^0$ .

$$s_e = \begin{cases} (-\alpha P_c)^{-\lambda} & \text{if } P_c \leq P_u \\ B(P_c) & \text{if } P_u < P_c < P_s \\ 1 & \text{if } P_s \leq P_c \end{cases} \quad (21)$$

551 where the breakpoints  $P_u$  and  $P_s$  satisfy  $P_u < P_c^0 < P_s \leq 0$ . The smoothing  
 552 polynomial

$$B(P_c) = b_0 + b_1(P_c - P_s) + b_2(P_c - P_s)^2 + b_3(P_c - P_s)^3 \quad (22)$$

553 introduces four more parameters, whose values follow from continuity. In particular  
 554 matching the saturated region requires  $B(P_s) = b_0 = 1$ , and a continuous derivative  
 555 at  $P_c = P_s$  requires  $B'(P_s) = b_1 = 0$ . Similarly, matching the value and derivative at  
 556  $P_c = P_u$  requires

$$b_2 = \frac{-1}{\Delta^2} \left[ 3 - (\alpha P_u)^{-\lambda} \left( 3 + \frac{\lambda \Delta}{P_u} \right) \right] \quad (23)$$

$$b_3 = \frac{-1}{\Delta^3} \left[ 2 - (\alpha P_u)^{-\lambda} \left( 2 + \frac{\lambda \Delta}{P_u} \right) \right] \quad (24)$$

557 where  $\Delta = P_u - P_s$ . Note  $P_u \leq \Delta < 0$ .

558 In practice, setting  $P_u$  too close to  $P_c^0$  can produce an unwanted local maximum  
 559 in the cubic smoothing regime, resulting in  $s_e > 1$ . Avoiding this condition requires  
 560 that  $B(P_c)$  increase monotonically from  $P_c = P_u$ , where  $B'(P_c) > 0$ , to  $P_c = P_s$ , where  
 561  $B'(P_c) = 0$ . Thus a satisfactory pair of breakpoints ensures

$$B'(P_c) = [P_c - P_s][2b_2 + 3b_3(P_c - P_s)] > 0 \quad (25)$$

562 throughout  $P_u \leq P_c < P_s$ .

563 Let  $P_c^*$  denote a local extremum of  $B$ , so that  $B'(P_c^*) = 0$ . If  $P_c^* \neq P_s$ , it follows  
 564  $P_c^* - P_s = -2b_2/(3b_3)$ . Rewriting equation 22,  $B'(P_c) = (P_c - P_s)3b_3(P_c - P_c^*)$  shows  
 565 that  $B'(P_c^*) > 0$  requires either: (1)  $b_3 < 0$  and  $P_c^* < P_u$ ; or (2)  $b_3 > 0$  and  $P_c^* > P_u$ .

567 The first possibility places  $P_c^*$  outside the cubic smoothing regime, and so does not  
 568 constrain the choice of  $P_u$  or  $P_s$ . The second possibility allows an unwanted local  
 569 extremum at  $P_u < P_c^* < P_s$ . In this case,  $b_3 > 0$  implies  $b_2 < 0$  (since  $P_c^* < P_s \leq 0$ ).  
 570 Then since  $B''(P_c^*) = -2b_2$ , the local extremum is a maximum, resulting in  $s_e(P_c^*) >$   
 571 1.

572 Given a breakpoint  $P_s$ , one strategy for choosing  $P_u$  is to guess a value, then  
 573 check whether the resulting  $b_2$  and  $b_3$  produces  $P_u < P_c^* < P_s$ . If so,  $P_u$  should be  
 574 made more negative. An alternative strategy is to choose  $P_u$  in order the guarantee  
 575 acceptable values for  $b_2$  and  $b_3$ . One convenient choice forces  $b_2 = 0$ . Another picks  
 576  $P_u$  in order to force  $b_3 = 0$ . Both of these reductions: (1) ensure  $B(P_c)$  has a positive  
 577 slope throughout the smoothing interval; (2) slightly reduce the computation cost of  
 578 finding  $s_e(P_c)$  for  $P_c$  on the smoothing interval; and (3) significantly reduce the  
 579 computational cost of inverting the model, in order to find  $P_c$  as a function of  $s_e$ .

580 As shown in Figure A 1, the two reductions differ mainly in that setting  $b_2 = 0$   
 581 seems to produce narrower smoothing regions (probably due to the fact that this  
 582 choice gives zero curvature at  $P_c = P_s$ , while  $b_3 = 0$  yields a negative second  
 583 derivative there). However, we have not verified this observation analytically.

584 Both reductions require solving a nonlinear expression either equation (23) or  
 585 (24), for  $P_u$ . While details are beyond the scope of this paper, we note that we have  
 586 used a bracketed Newton-Raphson's method. The search switches to bisection when  
 587 Newton-Raphson would jump outside the bounds established by previous iterations,  
 588 and by the requirement  $P_u < P_c^0$ . In any event, since the result of this calculation may  
 589 be cached for use throughout the simulation, it need not be particularly efficient.

## 590 5.2 Residual equation of VSFM formulation

591 The residual equation for the VSFM formulation at  $t + 1$  time level for  $n$ -th control  
 592 volume is given by

$$R_n^{t+1} \equiv \left( \frac{(\phi s_w \rho)_n^{t+1} - (\phi s_w \rho)_n^t}{\Delta t} \right) V_n + \sum_{n'} (\rho \mathbf{q})_{nn'}^{t+1} \cdot \mathbf{A}_{nn'} + Q_n^{t+1} V_n = 0 \quad (26)$$

593 where  $\phi$  [mm<sup>3</sup> mm<sup>3</sup>] is the soil porosity,  $s_w$  [-] is saturation,  $\rho$  [kg m<sup>-3</sup>] is water  
 594 density,  $\vec{q}_{nn'}$  [m s<sup>-1</sup>] is the Darcy flow velocity between  $n$ -th and  $n'$ -th control

595 volumes,  $A_{nn'}$  [m<sup>2</sup>] is the interface face area between  $n$ -th and  $n'$ -th control  
 596 volumes  $Q$  [kg m<sup>-3</sup> s<sup>-1</sup>] is a sink of water. The Darcy velocity is computed as

$$\mathbf{q}_{nn'} = - \left( \frac{\kappa k_r}{\mu} \right)_{nn'} \left[ \frac{P_{n'} - P_n - \rho_{nn'}(\mathbf{g} \cdot \mathbf{d}_{nn'})}{d_n + d_{n'}} \right] \mathbf{n}_{nn'} \quad (27)$$

597 where  $\kappa$  [m<sup>2</sup>] is intrinsic permeability,  $\kappa_r$  [-] is relative permeability,  $\mu$  [Pa s] is  
 598 viscosity of water,  $P$  [Pa] is pressure,  $\mathbf{g}$  [m s<sup>-2</sup>] is the acceleration due to gravity,  
 599  $d_n$  [m] and  $d_{n'}$  [m] is distance between centroid of  $n$ -th and  $n'$ -th control volume to  
 600 the common interface between the two control volumes,  $\mathbf{d}_{nn'}$  is a distance vector  
 601 joining centroid of  $n$ -th and  $n'$ -th control volume, and  $\mathbf{n}_{nn'}$  is a unit normal vector  
 602 joining centroid of  $n$ -th and  $n'$ -th control volume.

603 The density at the interface of control volume,  $\rho_{nn'}$ , is computed as inverse  
 604 distance weighted average by

$$\rho_{nn'} = \omega_{n'} \rho_n + \omega_n \rho_{n'} \quad (28)$$

605 where  $\omega_n$  and  $\omega_{n'}$  are given by

$$\omega_n = \frac{d_{n'}}{d_n + d_{n'}} = (1 - \omega_{n'}) \quad (29)$$

606 The first term on the RHS of equation 27 is computed as the product of distance  
 607 weighted harmonic average of intrinsic permeability,  $k_{nn'}$ , and upwinding of  
 608  $k_r/\mu$  ( $= \lambda$ ) as

$$\left( \frac{\kappa k_r}{\mu} \right)_{nn'} = k_{nn'} \left( \frac{k_r}{\mu} \right)_{nn'} = \left[ \frac{k_n k_{n'} (d_n + d_{n'})}{k_n d_{n'} + k_{n'} d_n} \right] \lambda_{nn'} \quad (30)$$

609 where

$$\lambda_{nn'} = \begin{cases} (k_r/\mu)_n & \text{if } \vec{q}_{nn'} > 0 \\ (k_r/\mu)_{n'} & \text{otherwise} \end{cases} \quad (31)$$

610 By substituting equation 28, 29 and 30 in equation 27, we obtain

$$\mathbf{q}_{nn'} = - \left[ \frac{k_n k_{n'}}{k_n d_{n'} + k_{n'} d_n} \right] \lambda_{nn'} [P_{n'} - P_n - \rho_{nn'}(\mathbf{g} \cdot \mathbf{d}_{nn'})] \mathbf{n}_{nn'} \quad (32)$$

611

### 612 5.3 Jacobian equation of VSFM formulation

613 The discretized equations of VSFM leads to a system of nonlinear equations given by

614  $\mathbf{R}^{t+1}(\mathbf{P}^{t+1}) = \mathbf{0}$ , which are solved using Newton's method using the Portable,

615 Extensible Toolkit for Scientific Computing (PETSc) library. The algorithm of  
 616 Newton's method requires solution of the following linear problem

$$\mathbf{J}^{t+1,k}(\mathbf{P}^{t+1,k}) \Delta \mathbf{P}^{t+1,k} = -\mathbf{R}^{t+1,k}(\mathbf{P}^{t+1,k}) \quad (33)$$

617 where  $\mathbf{J}^{t+1,k}(\mathbf{P}^{t+1,k})$  is the Jacobian matrix. In VFSM, the Jacobian matrix is  
 618 computed analytically. The contribution to the diagonal and off-diagonal entry of the  
 619 Jacobian matrix from  $n$ -th residual equations are given by

$$J_{nn} = \frac{\partial R_n}{\partial P_n} = \left( \frac{V_n}{\Delta t} \right) \frac{\partial(\rho \phi s_w)}{\partial P_n} + \sum_{n'} \frac{\partial(\rho \mathbf{q})_{nn'}}{\partial P_n} \mathbf{A}_{nn'} + \frac{\partial Q_n^{t+1}}{\partial P_n} V_n \quad (34)$$

$$J_{nn'} = \frac{\partial R_n}{\partial P_{n'}} = \sum_{n'} \frac{\partial(\rho \mathbf{q})_{nn'}}{\partial P_{n'}} \mathbf{A}_{nn'} + \frac{\partial Q_n^{t+1}}{\partial P_{n'}} V_n \quad (35)$$

620 The derivative of the accumulation term in  $J_{nn}$  is computed as

$$\frac{\partial(\rho \phi s_w)}{\partial P_n} = \phi s_w \frac{\partial \rho}{\partial P_n} + \rho s_w \frac{\partial \phi}{\partial P_n} + \rho \phi \frac{\partial s_w}{\partial P_n} \quad (36)$$

621 The derivative of flux between  $n$ -th and  $n'$ -th control volume with respect to  
 622 pressure of each control volume is given as

$$\frac{\partial(\rho \mathbf{q})_{nn'}}{\partial P_n} = \rho_{nn'} \frac{\partial \mathbf{q}_{nn'}}{\partial P_n} + \mathbf{q}_{nn'} \omega_n \frac{\partial \rho_n}{\partial P_n} \quad (37)$$

623

$$\frac{\partial(\rho \mathbf{q})_{nn'}}{\partial P_{n'}} = \rho_{nn'} \frac{\partial \mathbf{q}_{nn'}}{\partial P_{n'}} + \mathbf{q}_{nn'} \omega_{n'} \frac{\partial \rho_{n'}}{\partial P_{n'}} \quad (38)$$

624 Lastly, the derivative of Darcy velocity between  $n$ -th and  $n'$ -th control volume with  
 625 respect to pressure of each control volume is given as

$$\frac{\partial \mathbf{q}_{nn'}}{\partial P_n} = \left[ \frac{k_n k_{n'}}{k_n d_{n'} + k_{n'} d_n} \right] \lambda_{nn'} \left[ 1 + \omega_n (\mathbf{g} \cdot \mathbf{d}_{nn'}) \frac{\partial \rho_n}{\partial P_n} \right] \mathbf{n}_{nn'} + \mathbf{q}_{nn'} \frac{\partial(\ln(\lambda_{nn'}))}{\partial P_n} \quad (39)$$

$$\begin{aligned} \frac{\partial \mathbf{q}_{nn'}}{\partial P_{n'}} &= \left[ \frac{k_n k_{n'}}{k_n d_{n'} + k_{n'} d_n} \right] \lambda_{nn'} \left[ -1 + \omega_n (\mathbf{g} \cdot \mathbf{d}_{nn'}) \frac{\partial \rho_{n'}}{\partial P_{n'}} \right] \mathbf{n}_{nn'} \\ &+ \mathbf{q}_{nn'} \frac{\partial(\ln(\lambda_{nn'}))}{\partial P_{n'}} \end{aligned} \quad (40)$$

626



|

## 627 **6 Code availability**

628 The standalone VSFM code is available at [https://github.com/MPP-LSM/MPP\\_Notes](https://github.com/MPP-LSM/MPP_Notes)  
629 [on how to run the VSFM for all benchmark problems and compare results against](#)  
630 [PFLOTRAN at https://bitbucket.org/gbisht/notes-for-gmd-2018-44](https://bitbucket.org/gbisht/notes-for-gmd-2018-44),  
631 [The research was performed using E3SM v1.0 and the code is available at](#)  
632 <https://github.com/E3SM-Project/E3SM>.

## 633 **7 Competing interests**

634 The authors declare that they have no conflict of interest.

635

## 636 **8 Acknowledgements**

637 This research was supported by the Director, Office of Science, Office of Biological  
638 and Environmental Research of the US Department of Energy under contract no. DE-  
639 AC02-05CH11231 as part of the Energy Exascale Earth System Model (E3SM)  
640 programs.  
641

Formatted: Header

Formatted: Justified

Deleted: The ELM-VSFM code will be made available with the public release of E3SM model in April, 2018.

Formatted: Font color: Auto

644 **9 Tables**645 **Table 1** [Soil properties used in the three test problems described in section](#)  
646 [2.3.](#)

<a href="#">Problem number</a>	$\phi$ [-]	$\lambda$ [-]	$\alpha$ [Pa <sup>-1</sup> ]	$k$ [m <sup>2</sup> ]
<a href="#">1</a>	<a href="#">0.368</a>	<a href="#">0.5</a>	<a href="#">3.4257x10<sup>-4</sup></a>	<a href="#">8.3913x10<sup>-12</sup></a>
<a href="#">2</a>	<a href="#">0.4</a>	<a href="#">0.5455</a>	<a href="#">4x10<sup>-4</sup></a>	<a href="#">2.5281x10<sup>-12</sup> (top layer)</a> <a href="#">2.5281x10<sup>-13</sup> (bottom layer)</a>
<a href="#">3</a>	<a href="#">0.368</a>	<a href="#">0.5</a>	<a href="#">3.4257x10<sup>-4</sup></a>	<a href="#">8.3913x10<sup>-12</sup></a>

647

648 **Table 2** Bias, root mean square error (RMSE), and correlation (R<sup>2</sup>) between  
649 simulated water table depth and Fan et al. (2013) data.

	<b>Bias</b> [m]	<b>RMSE</b> [m]	<b>R<sup>2</sup></b>
For all grids in ELM simulation with default $f_{drain}$	-10.3	21.3	0.28
For all grids in ELM simulation with optimal $f_{drain}$	2.10	8.33	0.91
For 79% grids with optimal $f_{drain}$ in ELM simulation with optimal $f_{drain}$	-0.04	0.67	0.99
For 21% grids without optimal $f_{drain}$ in ELM simulation with optimal $f_{drain}$	-9.82	18.08	0.31

650

651

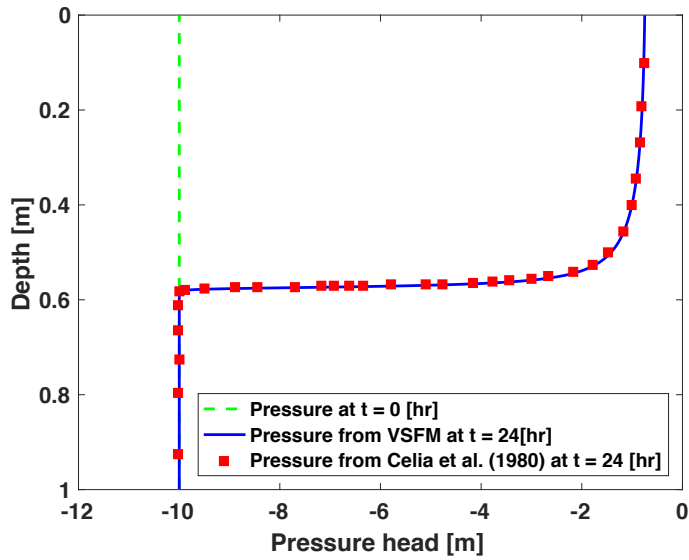
652 **Table 3 ILAMB benchmark scores for latent heat flux (LH), sensible heat flux**  
 653 **(SH), total water storage anomaly (TWSA), and surface runoff. The calculation**  
 654 **of ILAMB metrics and scores are described at <http://redwood.ess.uci.edu/>.**

	Data Source	Simulation with default $f_d$			Simulation with optimal $f_d$		
		Bias	RMSE	ILAMB Score	Bias	RMSE	ILAMB Score
LH	FLUXNET	10.1 [Wm <sup>-2</sup> ]	21.0 [Wm <sup>-2</sup> ]	0.68	9.5 [Wm <sup>-2</sup> ]	21.3 [Wm <sup>-2</sup> ]	0.68
	GBAF	7.1 [Wm <sup>-2</sup> ]	16.3 [Wm <sup>-2</sup> ]	0.81	6.3 [Wm <sup>-2</sup> ]	16.3 [Wm <sup>-2</sup> ]	0.81
SH	FLUXNET	6.7 [Wm <sup>-2</sup> ]	22.5 [Wm <sup>-2</sup> ]	0.66	7.1 [Wm <sup>-2</sup> ]	22.8 [Wm <sup>-2</sup> ]	0.65
	GBAF	6.9 [Wm <sup>-2</sup> ]	21.2 [Wm <sup>-2</sup> ]	0.71	7.6 [Wm <sup>-2</sup> ]	21.7 [Wm <sup>-2</sup> ]	0.70
TWSA	GRACE	1.3 [cm]	7.8 [cm]	0.48	3.0 [cm]	9.6 [cm]	0.48
Runoff	Dai	-0.26 [kg m <sup>-2</sup> d <sup>-1</sup> ]	0.91 [m <sup>2</sup> m <sup>-2</sup> d <sup>-1</sup> ]	0.52	-0.23 [kg m <sup>-2</sup> d <sup>-1</sup> ]	0.88 [kg m <sup>-2</sup> d <sup>-1</sup> ]	0.50

655

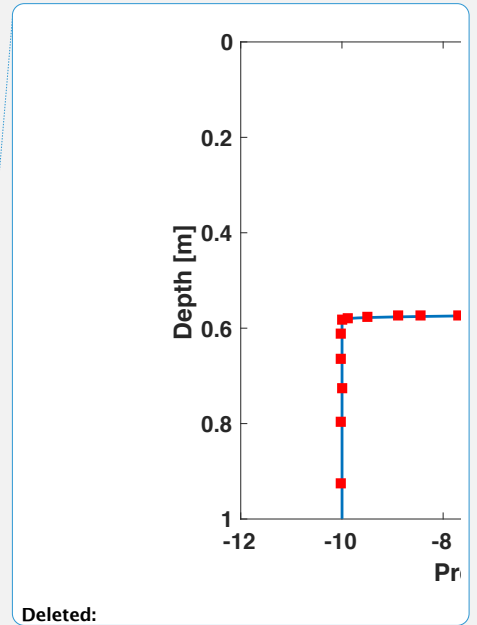
656

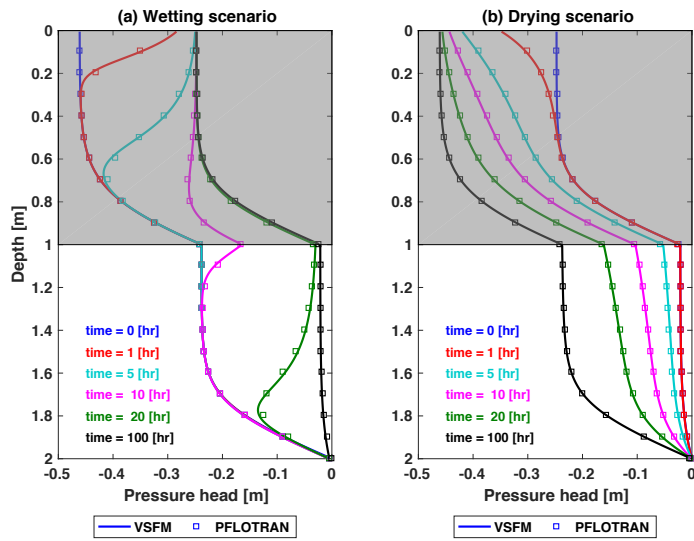
657 10 Figures



658

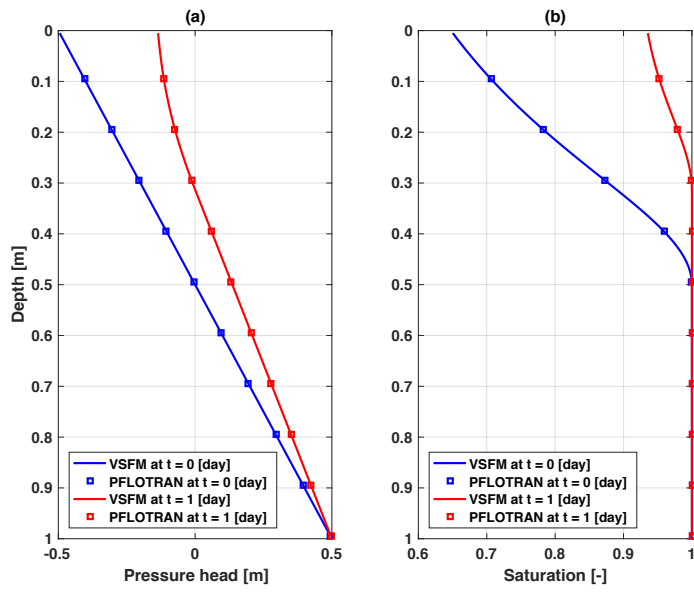
659 **Figure 1. Comparison of VFSM simulated pressure profile (blue line) against**  
660 **data (red square) reported in Celia et al. (1990) at time = 24 hr for infiltration**  
661 **in a dry soil column. Initial pressure condition is shown by green line.**





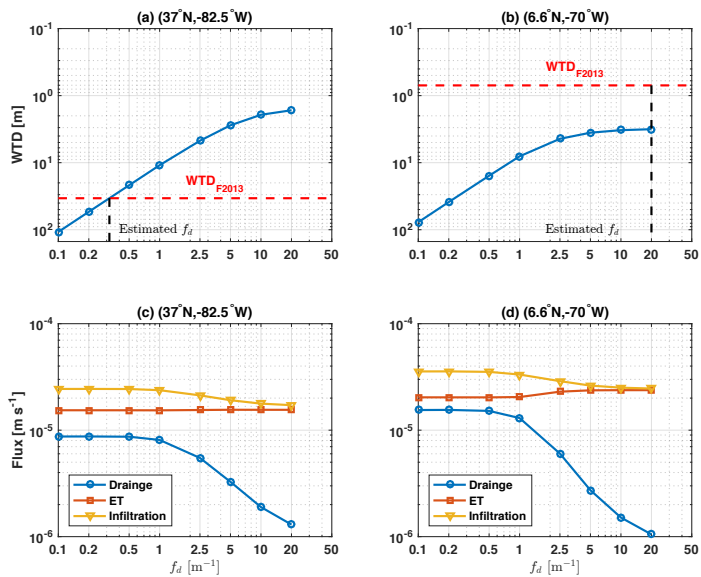
663

664 **Figure 2. Transient liquid pressure simulated for a two layer soil system by**  
665 **VSFM (solid line) and PFLOTRAN (square) for wetting (left) and drying (right)**  
666 **scenarios.**



667

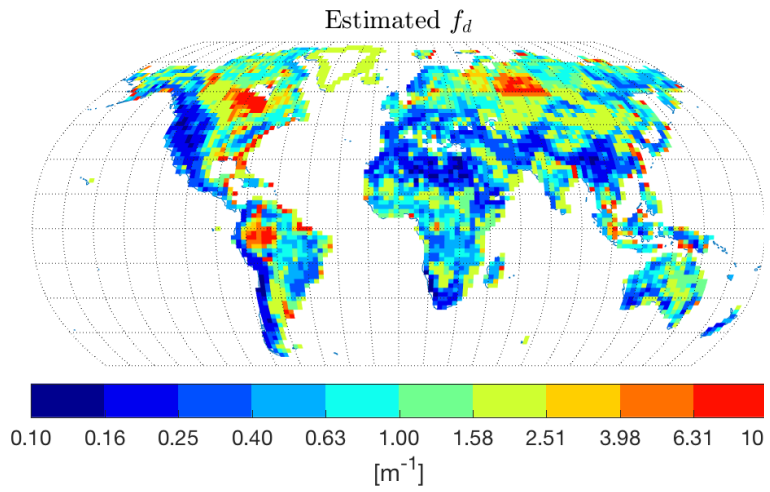
668 **Figure 3. Transient liquid pressure (a) and soil saturation (b) simulated by**  
669 **VSFM (solid line) and PFLOTRAN (square) for the water table dynamics test**  
670 **problem.**



671

672 **Figure 4. (a-b) The nonlinear relationship between simulated water table**  
 673 **depth (WTD) and  $f_d$  for two gridcells within ELM's global grid. WTD from the**  
 674 **Fan et al. (2013) dataset and optimal  $f_d$  for the two gridcells are shown with a**  
 675 **dashed red and dashed black lines, respectively. (c-d) The simulated drainage,**  
 676 **evapotranspiration, and infiltration fluxes as functions of optimal  $f_d$  for the**  
 677 **two ELM gridcells.**

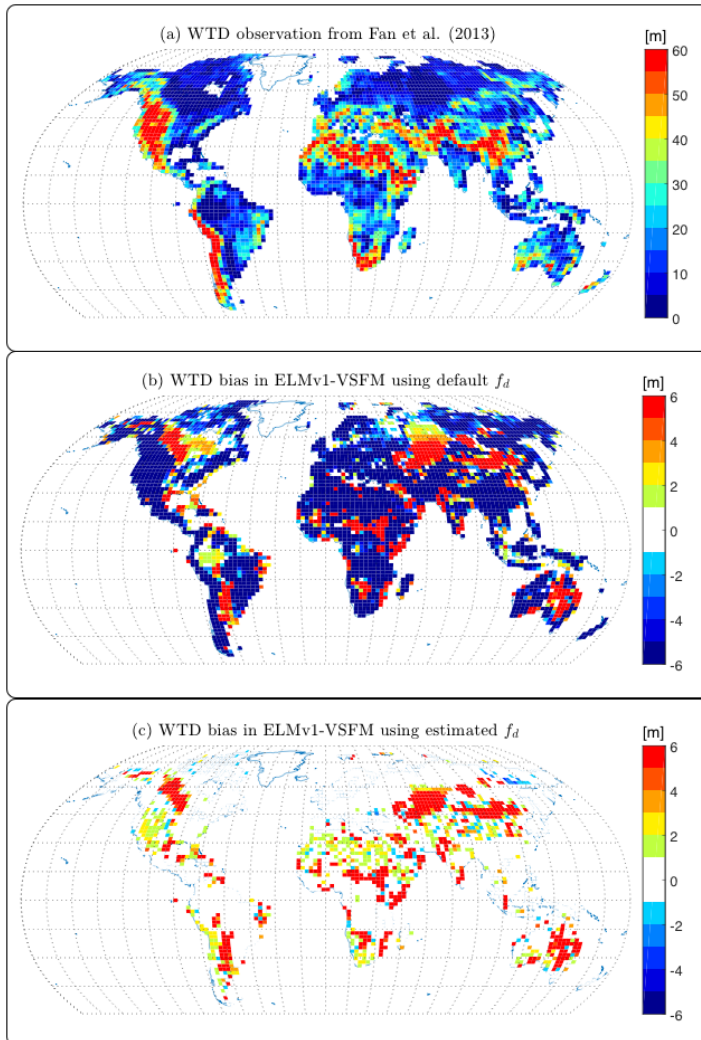
678



679

680 **Figure 5. Global estimate of  $f_d$ .**

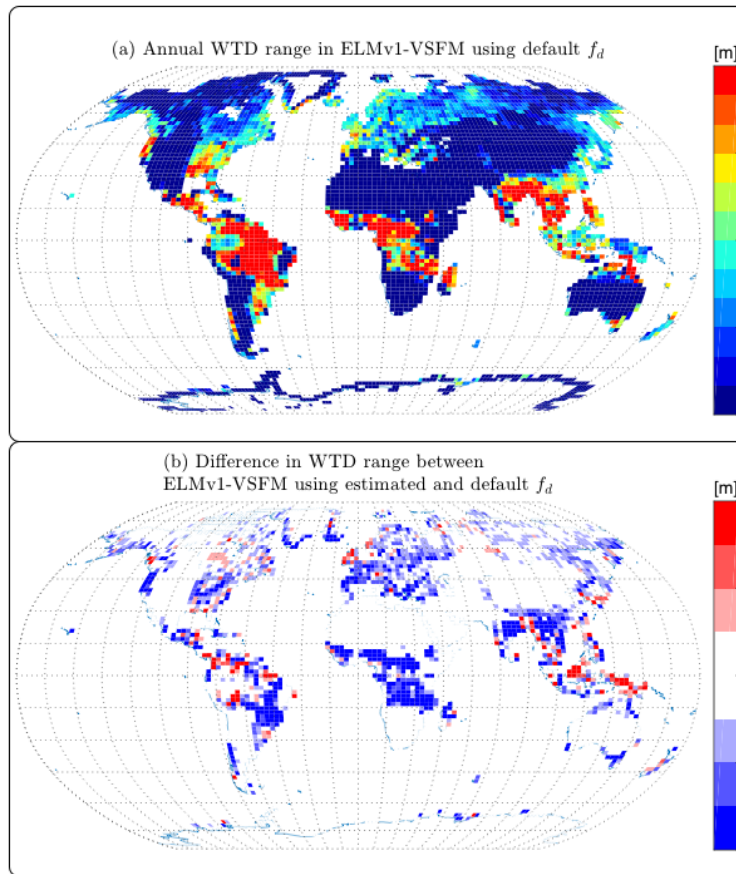




681

682 **Figure 6. (a) Water table depth observation from Fan et al. (2013); (b) Water**  
683 **table depth biases (=Model - Obs) from ELMv1-VSFM using default spatially**  
684 **homogeneous  $f_d$ ; and (c) Water table depth biases from ELMv1-VSFM using**  
685 **spatially heterogeneous  $f_d$ .**

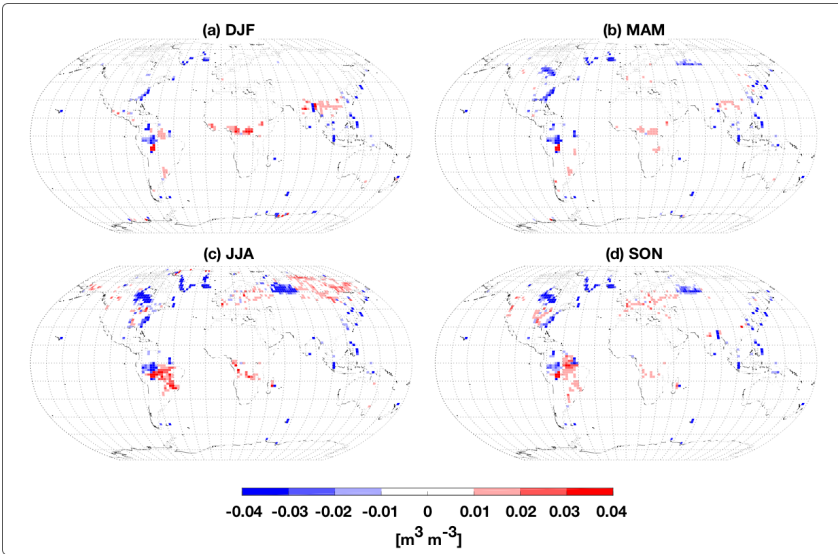
686



687

688 **Figure 7. (a) Annual range of water table depth for ELMv1-VSFM simulation**689 **with spatially heterogeneous estimates of  $f_d$  and (b) Difference in annual**690 **water table depth range between simulations with optimal and default  $f_d$ .**

691



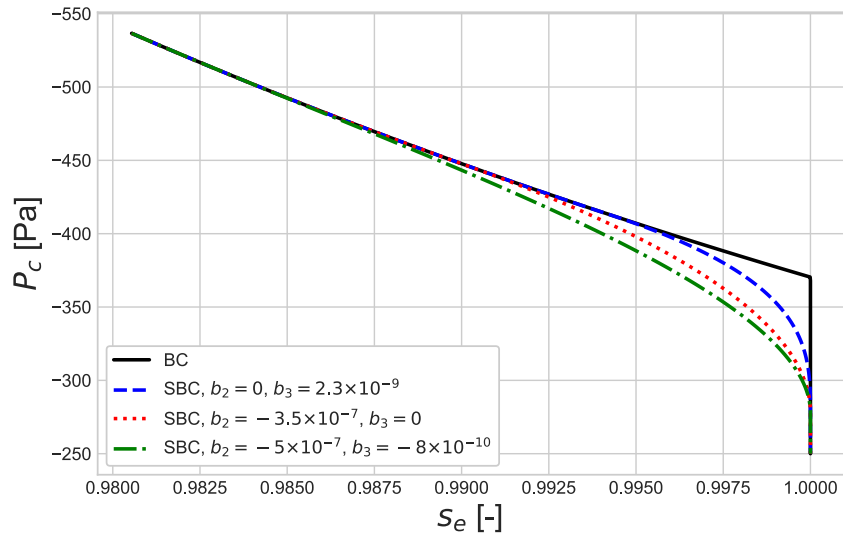
692

693 **Figure 8. Seasonal monthly mean soil moisture differences for top 10 cm**

694 **between ELMv1-VSFM simulations with optimal and default  $f_d$  values.**

695

696



697

698 **Figure A 1** The Brooks-Corey water rendition curve for estimating liquid saturation,  $s_e$ ,  
699 as a function of capillary pressure,  $P_c$ , shown in solid black line and smooth  
700 approximation of Brooks-Corey (SBC) are shown in dashed line.

701

702 **References**

703 Alkhaier, F., Flerchinger, G. N., and Su, Z.: Shallow groundwater effect on land surface  
704 temperature and surface energy balance under bare soil conditions: modeling and  
705 description, *Hydrol. Earth Syst. Sci.*, 16, 1817-1831, 2012.

706 Alley, W. M.: Ground Water and Climate, *Ground Water*, 39, 161-161, 2001.

707 [Amenu, G. G. and Kumar, P.: A model for hydraulic redistribution incorporating  
708 coupled soil-root moisture transport, \*Hydrol. Earth Syst. Sci.\*, 12, 55-74, 2008.](#)

709 Anyah, R. O., Weaver, C. P., Miguez-Macho, G., Fan, Y., and Robock, A.: Incorporating  
710 water table dynamics in climate modeling: 3. Simulated groundwater influence on  
711 coupled land-atmosphere variability, *Journal of Geophysical Research: Atmospheres*,  
712 113, n/a-n/a, 2008.

713 Balay, S., Abhyankar, S., Adams, M. F., Brown, J., Brune, P., Buschelman, K., Dalcin, L.,  
714 Eijkhout, V., Gropp, W. D., Kaushik, D., Knepley, M. G., McInnes, L. C., Rupp, K., Smith,  
715 B. F., Zampini, S., Zhang, H., and Zhang, H.: PETSc Users Manual, Argonne National  
716 Laboratory ANL-95/11 - Revision 3.7, 1-241 pp., 2016.

717 Banks, E. W., Brunner, P., and Simmons, C. T.: Vegetation controls on variably  
718 saturated processes between surface water and groundwater and their impact on the  
719 state of connection, *Water Resources Research*, 47, n/a-n/a, 2011.

720 [Bense, V. F., Kooi, H., Ferguson, G., and Read, T.: Permafrost degradation as a control  
721 on hydrogeological regime shifts in a warming climate, \*Journal of Geophysical  
722 Research: Earth Surface\*, 117, 2012.](#)

723 Bernhardt, M., Schulz, K., Liston, G. E., and Zängl, G.: The influence of lateral snow  
724 redistribution processes on snow melt and sublimation in alpine regions, *Journal of  
725 Hydrology*, 424-425, 196-206, 2012.

726 Beven, K. J. and Kirkby, M. J.: A physically based, variable contributing area model of  
727 basin hydrology / Un modèle à base physique de zone d'appel variable de l'hydrologie  
728 du bassin versant, *Hydrological Sciences Bulletin*, 24, 43-69, 1979.

729 Bisht, G., Huang, M., Zhou, T., Chen, X., Dai, H., Hammond, G. E., Riley, W. J., Downs, J. L.,  
730 Liu, Y., and Zachara, J. M.: Coupling a three-dimensional subsurface flow and transport  
731 model with a land surface model to simulate stream-aquifer-land interactions  
732 (CP v1.0), *Geosci. Model Dev.*, 10, 4539-4562, 2017.

733 Bisht, G., Riley, W. J., Wainwright, H. M., Dafflon, B., Yuan, F., and Romanovsky, V. E.:  
734 Impacts of microtopographic snow redistribution and lateral subsurface processes  
735 on hydrologic and thermal states in an Arctic polygonal ground ecosystem: a case  
736 study using ELM-3D v1.0, *Geosci. Model Dev.*, 11, 61-76, 2018.

737 [Bohrer, G., Mourad, H., Laursen, T. A., Drewry, D., Avissar, R., Poggi, D., Oren, R., and  
738 Katul, G. G.: Finite element tree crown hydrodynamics model \(FETCH\) using porous  
739 media flow within branching elements: A new representation of tree hydrodynamics,  
740 \*Water Resources Research\*, 41, n/a-n/a, 2005.](#)

741 Brooks, R. H. and Corey, A. T.: Hydraulic properties of porous media, Colorado State  
742 University, Fort Collins, CO, 1964.

743 [Brown, J., Knepley, M. G., May, D. A., McInnes, L. C., and Smith, B.: Composable linear  
744 solvers for multiphysics, 2012, 55-62.](#)

745 Brunke, M. A., Broxton, P., Pelletier, J., Gochis, D., Hazenberg, P., Lawrence, D. M.,  
746 Leung, L. R., Niu, G.-Y., Troch, P. A., and Zeng, X.: Implementing and Evaluating Variable

Formatted: Header

Formatted: Font color: Auto

Formatted: Font color: Auto

Formatted: Font color: Auto

Formatted: Font color: Auto

Formatted: Font color: Auto

Formatted: Header

747 Soil Thickness in the Community Land Model, Version 4.5 (CLM4.5), Journal of  
748 Climate, 29, 3441-3461, 2016.

749 Celia, M. A., Bouloutas, E. T., and Zarba, R. L.: A general mass-conservative numerical  
750 solution for the unsaturated flow equation, Water Resources Research, 26, 1483-  
751 1496, 1990.

752 Chen, J. and Kumar, P.: Topographic Influence on the Seasonal and Interannual  
753 Variation of Water and Energy Balance of Basins in North America, Journal of Climate,  
754 14, 1989-2014, 2001.

755 Chen, X. and Hu, Q.: Groundwater influences on soil moisture and surface evaporation,  
756 Journal of Hydrology, 297, 285-300, 2004.

757 Chen, Y., Chen, Y., Xu, C., Ye, Z., Li, Z., Zhu, C., and Ma, X.: Effects of ecological water  
758 conveyance on groundwater dynamics and riparian vegetation in the lower reaches  
759 of Tarim River, China, Hydrological Processes, 24, 170-177, 2010.

760 Clapp, R. B. and Hornberger, G. M.: Empirical equations for some soil hydraulic  
761 properties, Water Resources Research, 14, 601-604, 1978.

762 [Clark, M. P., Fan, Y., Lawrence, D. M., Adam, J. C., Bolster, D., Gochis, D. J., Hooper, R. P.,](#)  
763 [Kumar, M., Leung, L. R., Mackay, D. S., Maxwell, R. M., Shen, C., Swenson, S. C., and Zeng,](#)  
764 [X.: Improving the representation of hydrologic processes in Earth System Models,](#)  
765 [Water Resources Research, 51, 5929-5956, 2015.](#)

766 [Collier, N., Hoffman, F. M., Lawrence, D. M., Keppel-Aleks, G., Koven, C. D., Riley, W.](#)  
767 [L., Mu, M., and Randerson, J. T.: The International Land 1 Model Benchmarking](#)  
768 [\(ILAMB\) System: Design, Theory, and Implementation, in review J. Advances in](#)  
769 [Modeling Earth Systems, 2018, 2018.](#)

770 Dai, A. and Trenberth, K. E.: Estimates of Freshwater Discharge from Continents:  
771 Latitudinal and Seasonal Variations, Journal of Hydrometeorology, 3, 660-687, 2002.

772 Dams, J., Woldeamlak, S. T., and Batelaan, O.: Predicting land-use change and its  
773 impact on the groundwater system of the Kleine Nete catchment, Belgium, Hydrol.  
774 Earth Syst. Sci., 12, 1369-1385, 2008.

775 [Dennis, J. M., Vertenstein, M., Worley, P. H., Mirin, A. A., Craig, A. P., Jacob, R., and](#)  
776 [Mickelson, S.: Computational performance of ultra-high-resolution capability in the](#)  
777 [Community Earth System Model, The International Journal of High Performance](#)  
778 [Computing Applications, 26, 5-16, 2012.](#)

779 [E3SM Project, D.: Energy Exascale Earth System Model, 2018.](#)

780 Fan, Y., Li, H., and Miguez-Macho, G.: Global Patterns of Groundwater Table Depth,  
781 Science, 339, 940-943, 2013.

782 Fan, Y., Miguez-Macho, G., Weaver, C. P., Walko, R., and Robock, A.: Incorporating  
783 water table dynamics in climate modeling: 1. Water table observations and  
784 equilibrium water table simulations, Journal of Geophysical Research: Atmospheres,  
785 112, n/a-n/a, 2007.

786 Farthing, M. W., Kees, C. E., and Miller, C. T.: Mixed finite element methods and higher  
787 order temporal approximations for variably saturated groundwater flow, Advances  
788 in Water Resources, 26, 373-394, 2003.

789 Ferguson, I. M. and Maxwell, R. M.: Human impacts on terrestrial hydrology: climate  
790 change versus pumping and irrigation, Environmental Research Letters, 7, 044022,  
791 2012.

Formatted: Font color: Auto

Formatted: Font color: Auto

792 [Frampton, A., Painter, S., Lyon, S. W., and Destouni, G.: Non-isothermal, three-phase](#)  
793 [simulations of near-surface flows in a model permafrost system under seasonal](#)  
794 [variability and climate change. \*Journal of Hydrology\*. 403, 352-359, 2011.](#)

795 [Ghimire, B., Riley, W. J., Koven, C. D., Mu, M., and Randerson, J. T.:](#) Representing leaf  
796 and root physiological traits in CLM improves global carbon and nitrogen cycling  
797 predictions, *Journal of Advances in Modeling Earth Systems*, 8, 598-613, 2016.

798 [Grant, R. F., Humphreys, E. R., and Lafleur, P. M.:](#) Ecosystem CO<sub>2</sub> and CH<sub>4</sub> exchange in  
799 a mixed tundra and a fen within a hydrologically diverse Arctic landscape: 1. Modeling  
800 versus measurements, *Journal of Geophysical Research: Biogeosciences*, 120, 1366-  
801 1387, 2015.

802 [Grant, R. F., Mekonnen, Z. A., Riley, W. J., Wainwright, H. M., Graham, D., and Torn, M.](#)  
803 [S.: Mathematical Modelling of Arctic Polygonal Tundra with Ecosys: 1.](#)  
804 [Microtopography Determines How Active Layer Depths Respond to Changes in](#)  
805 [Temperature and Precipitation. \*Journal of Geophysical Research: Biogeosciences\*,](#)  
806 [122, 3161-3173, 2017.](#)

807 [Green, T. R., Taniguchi, M., Kooi, H., Gurdak, J. J., Allen, D. M., Hiscock, K. M., Treidel, H.,](#)  
808 [and Aureli, A.:](#) Beneath the surface of global change: Impacts of climate change on  
809 groundwater, *Journal of Hydrology*, 405, 532-560, 2011.

810 [Gutmann, E. D. and Small, E. E.:](#) [The effect of soil hydraulic properties vs. soil texture](#)  
811 [in land surface models. \*Geophysical Research Letters\*. 32, 2005.](#)

812 [Hammond, G. E. and Lichtner, P. C.:](#) Field-scale model for the natural attenuation of  
813 uranium at the Hanford 300 Area using high-performance computing, *Water*  
814 *Resources Research*, 46, n/a-n/a, 2010.

815 [Hilberts, A. G. J., Troch, P. A., and Paniconi, C.:](#) Storage-dependent drainable porosity  
816 for complex hillslopes, *Water Resources Research*, 41, n/a-n/a, 2005.

817 [Hoffman, F. M., Koven, C. D., Keppel-Aleks, G., Lawrence, D. M., Riley, W. J., Randerson,](#)  
818 [J. T., Ahlstrom, A., Abramowitz, G., Baldocchi, D. D., Best, M. J., Bond-Lamberty, B.,](#)  
819 [Kauwe}, M. G. D., Denning, A. S., Desai, A. R., Eyring, V., Fisher, J. B., Fisher, R. A.,](#)  
820 [Gleckler, P. J., Huang, M., Hugelius, G., Jain, A. K., Kiang, N. Y., Kim, H., Koster, R. D.,](#)  
821 [Kumar, S. V., Li, H., Luo, Y., Mao, J., McDowell, N. G., Mishra, U., Moorcroft, P. R., Pau, G.](#)  
822 [S. H., Ricciuto, D. M., Schaefer, K., Schwalm, C. R., Serbin, S. P., Shevliakova, E., Slater,](#)  
823 [A. G., Tang, J., Williams, M., Xia, J., Xu, C., Joseph, R., and Koch, D.:](#) International Land  
824 Model Benchmarking (ILAMB) 2016 Workshop Report, U.S. Department of Energy,  
825 Office of Science, 159 pp., 2017.

826 [Hou, Z., Huang, M., Leung, L. R., Lin, G., and Ricciuto, D. M.:](#) Sensitivity of surface flux  
827 simulations to hydrologic parameters based on an uncertainty quantification  
828 framework applied to the Community Land Model, *Journal of Geophysical Research:*  
829 *Atmospheres*, 117, n/a-n/a, 2012.

830 [Hwang, T., Band, L. E., Vose, J. M., and Tague, C.:](#) Ecosystem processes at the watershed  
831 scale: Hydrologic vegetation gradient as an indicator for lateral hydrologic  
832 connectivity of headwater catchments, *Water Resources Research*, 48, n/a-n/a, 2012.

833 [Ji, P., Yuan, X., and Liang, X.-Z.:](#) Do Lateral Flows Matter for the Hyperresolution Land  
834 Surface Modeling?, *Journal of Geophysical Research: Atmospheres*, doi:  
835 10.1002/2017JD027366, 2017. n/a-n/a, 2017.

Formatted: Header

Formatted: Font color: Auto

Formatted: Font color: Auto

Formatted: Font color: Auto

Jiang, X., Niu, G.-Y., and Yang, Z.-L.: Impacts of vegetation and groundwater dynamics on warm season precipitation over the Central United States, *Journal of Geophysical Research: Atmospheres*, 114, n/a-n/a, 2009.

Jung, M., Reichstein, M., and Bondeau, A.: Towards global empirical upscaling of FLUXNET eddy covariance observations: validation of a model tree ensemble approach using a biosphere model, *Biogeosciences*, 6, 2001-2013, 2009.

[Kane, D. L., Hinkel, K. M., Goering, D. J., Hinzman, L. D., and Outcalt, S. I.: Non-conductive heat transfer associated with frozen soils, \*Global and Planetary Change\*, 29, 275-292, 2001.](#)

Kees, C. E. and Miller, C. T.: Higher order time integration methods for two-phase flow, *Advances in Water Resources*, 25, 159-177, 2002.

Kim, H., Yeh, P. J. F., Oki, T., and Kanae, S.: Role of rivers in the seasonal variations of terrestrial water storage over global basins, *Geophysical Research Letters*, 36, n/a-n/a, 2009.

Kollet, S. J. and Maxwell, R. M.: Capturing the influence of groundwater dynamics on land surface processes using an integrated, distributed watershed model, *Water Resources Research*, 44, n/a-n/a, 2008.

Koster, R. D., Suarez, M. J., Ducharne, A., Stieglitz, M., and Kumar, P.: A catchment-based approach to modeling land surface processes in a general circulation model: 1. Model structure, *Journal of Geophysical Research: Atmospheres*, 105, 24809-24822, 2000.

Kundzewicz, Z. W. and Doli, P.: Will groundwater ease freshwater stress under climate change?, *Hydrological Sciences Journal*, 54, 665-675, 2009.

Lasslop, G., Reichstein, M., Papale, D., Richardson, A. D., Arneeth, A., Barr, A., Stoy, P., and Wohlfahrt, G.: Separation of net ecosystem exchange into assimilation and respiration using a light response curve approach: critical issues and global evaluation, *Global Change Biology*, 16, 187-208, 2010.

Leng, G., Huang, M., Tang, Q., and Leung, L. R.: A modeling study of irrigation effects on global surface water and groundwater resources under a changing climate, *Journal of Advances in Modeling Earth Systems*, 7, 1285-1304, 2015.

Leng, G., Leung, L. R., and Huang, M.: Significant impacts of irrigation water sources and methods on modeling irrigation effects in the ACMEland Model, *Journal of Advances in Modeling Earth Systems*, 9, 1665-1683, 2017.

Leung, L. R., Huang, M., Qian, Y., and Liang, X.: Climate-soil-vegetation control on groundwater table dynamics and its feedbacks in a climate model, *Climate Dynamics*, 36, 57-81, 2011.

Levine, J. B. and Salvucci, G. D.: Equilibrium analysis of groundwater-vadose zone interactions and the resulting spatial distribution of hydrologic fluxes across a Canadian Prairie, *Water Resources Research*, 35, 1369-1383, 1999.

Liang, X., Xie, Z., and Huang, M.: A new parameterization for surface and groundwater interactions and its impact on water budgets with the variable infiltration capacity (VIC) land surface model, *Journal of Geophysical Research: Atmospheres*, 108, n/a-n/a, 2003.

Lohse, K. A., Brooks, P. D., McIntosh, J. C., Meixner, T., and Huxman, T. E.: Interactions Between Biogeochemistry and Hydrologic Systems, *Annual Review of Environment and Resources*, 34, 65-96, 2009.



882 [Manoli, G., Bonetti, S., Domec, J.-C., Putti, M., Katul, G., and Marani, M.: Tree root](#)  
883 [systems competing for soil moisture in a 3D soil-plant model. \*Advances in Water\*](#)  
884 [Resources, 66, 32-42, 2014.](#)

885 Marvel, K., Biasutti, M., Bonfils, C., Taylor, K. E., Kushnir, Y., and Cook, B. I.: Observed  
886 and Projected Changes to the Precipitation Annual Cycle, *Journal of Climate*, 30, 4983-  
887 4995, 2017.

888 Maxwell, R. M. and Miller, N. L.: Development of a Coupled Land Surface and  
889 Groundwater Model, *Journal of Hydrometeorology*, 6, 233-247, 2005.

890 [McDowell, N. G. and Allen, C. D.: Darcy's law predicts widespread forest mortality](#)  
891 [under climate warming. \*Nature Clim. Change\*, 5, 669-672, 2015.](#)

892 Miguez-Macho, G., Fan, Y., Weaver, C. P., Walko, R., and Robock, A.: Incorporating  
893 water table dynamics in climate modeling: 2. Formulation, validation, and soil  
894 moisture simulation, *Journal of Geophysical Research: Atmospheres*, 112, n/a-n/a,  
895 2007.

896 Milly, P. C. D., Malyshev, S. L., Shevliakova, E., Dunne, K. A., Findell, K. L., Gleeson, T.,  
897 Liang, Z., Philipps, P., Stouffer, R. J., and Swenson, S.: An Enhanced Model of Land  
898 Water and Energy for Global Hydrologic and Earth-System Studies, *Journal of*  
899 *Hydrometeorology*, 15, 1739-1761, 2014.

900 Mualem, Y.: A new model for predicting the hydraulic conductivity of unsaturated  
901 porous media, *Water Resources Research*, 12, 513-522, 1976.

902 Niu, G.-Y., Yang, Z.-L., Dickinson, R. E., and Gulden, L. E.: A simple TOPMODEL-based  
903 runoff parameterization (SIMTOP) for use in global climate models, *Journal of*  
904 *Geophysical Research: Atmospheres*, 110, n/a-n/a, 2005.

905 Niu, G.-Y., Yang, Z.-L., Dickinson, R. E., Gulden, L. E., and Su, H.: Development of a simple  
906 groundwater model for use in climate models and evaluation with Gravity Recovery  
907 and Climate Experiment data, *Journal of Geophysical Research: Atmospheres*, 112,  
908 n/a-n/a, 2007.

909 Niu, J., Shen, C., Chambers, J. Q., Melack, J. M., and Riley, W. J.: Interannual Variation in  
910 Hydrologic Budgets in an Amazonian Watershed with a Coupled Subsurface-Land  
911 Surface Process Model, *Journal of Hydrometeorology*, 18, 2597-2617, 2017.

912 Oleson, K. W., D.M. Lawrence, G.B. Bonan, B. Drewniak, M. Huang, C.D. Koven, S. Levis,  
913 F. Li, W.J. Riley, Z.M. Subin, S.C. Swenson, P.E. Thornton, A. Bozbiyik, R. Fisher, E.  
914 Kluzek, J.-F. Lamarque, P.J. Lawrence, L.R. Leung, W. Lipscomb, S. Muszala, D.M.  
915 Ricciuto, W. Sacks, Y. Sun, J. Tang, Z.-L. Yang: Technical Description of version 4.5 of  
916 the Community Land Model (CLM), National Center for Atmospheric Research,  
917 Boulder, CO, 422 pp., 2013.

918 Pacific, V. J., McGlynn, B. L., Riveros-Iregui, D. A., Welsch, D. L., and Epstein, H. E.:  
919 Landscape structure, groundwater dynamics, and soil water content influence soil  
920 respiration across riparian-hillslope transitions in the Tenderfoot Creek  
921 Experimental Forest, Montana, *Hydrological Processes*, 25, 811-827, 2011.

922 Pelletier, J. D., Broxton, P. D., Hazenberg, P., Zeng, X., Troch, P. A., Niu, G.-Y., Williams,  
923 Z., Brunke, M. A., and Gochis, D.: A gridded global data set of soil, intact regolith, and  
924 sedimentary deposit thicknesses for regional and global land surface modeling,  
925 *Journal of Advances in Modeling Earth Systems*, 8, 41-65, 2016.

Formatted: Header

Formatted: Font color: Auto

Formatted: Font color: Auto

- 926 Petra, D.: Vulnerability to the impact of climate change on renewable groundwater  
927 resources: a global-scale assessment, *Environmental Research Letters*, 4, 035006,  
928 2009.
- 929 Piao, S. L., Ito, A., Li, S. G., Huang, Y., Ciais, P., Wang, X. H., Peng, S. S., Nan, H. J., Zhao, C.,  
930 Ahlström, A., Andres, R. J., Chevallier, F., Fang, J. Y., Hartmann, J., Huntingford, C., Jeong,  
931 S., Levis, S., Levy, P. E., Li, J. S., Lomas, M. R., Mao, J. F., Mayorga, E., Mohammat, A.,  
932 Muraoka, H., Peng, C. H., Peylin, P., Poulter, B., Shen, Z. H., Shi, X., Sitch, S., Tao, S., Tian,  
933 H. Q., Wu, X. P., Xu, M., Yu, G. R., Viogy, N., Zaehle, S., Zeng, N., and Zhu, B.: The carbon  
934 budget of terrestrial ecosystems in East Asia over the last two decades,  
935 *Biogeosciences*, 9, 3571-3586, 2012.
- 936 Pruess, K., Oldenburg, C., and Moridis, G.: TOUGH2 User's Guide, Version 2.0,  
937 Lawrence Berkeley National Laboratory, Berkeley, CALBNL-43134, 1999.
- 938 Rihani, J. F., Maxwell, R. M., and Chow, F. K.: Coupling groundwater and land surface  
939 processes: Idealized simulations to identify effects of terrain and subsurface  
940 heterogeneity on land surface energy fluxes, *Water Resources Research*, 46, n/a-n/a,  
941 2010.
- 942 Salvucci, G. D. and Entekhabi, D.: Hillslope and Climatic Controls on Hydrologic Fluxes,  
943 *Water Resources Research*, 31, 1725-1739, 1995.
- 944 Shen, C., Niu, J., and Phanikumar, M. S.: Evaluating controls on coupled hydrologic and  
945 vegetation dynamics in a humid continental climate watershed using a subsurface-  
946 land surface processes model, *Water Resources Research*, 49, 2552-2572, 2013.
- 947 Siebert, S., Burke, J., Faures, J. M., Frenken, K., Hoogeveen, J., Döll, P., and Portmann, F.  
948 T.: Groundwater use for irrigation – a global inventory, *Hydrol. Earth Syst. Sci.*, 14,  
949 1863-1880, 2010.
- 950 Sivapalan, M., Beven, K., and Wood, E. F.: On hydrologic similarity: 2. A scaled model  
951 of storm runoff production, *Water Resources Research*, 23, 2266-2278, 1987.
- 952 Soylu, M. E., Istanbuluoglu, E., Lenters, J. D., and Wang, T.: Quantifying the impact of  
953 groundwater depth on evapotranspiration in a semi-arid grassland region, *Hydrol.*  
954 *Earth Syst. Sci.*, 15, 787-806, 2011.
- 955 [Sperry, J. S., Adler, F. R., Campbell, G. S., and Comstock, J. P.: Limitation of plant water  
956 use by rhizosphere and xylem conductance: results from a model, \*Plant, Cell &  
957 Environment\*, 21, 347-359, 1998.](#)
- 958 Srivastava, R. and Yeh, T. C. J.: Analytical solutions for one-dimensional, transient  
959 infiltration toward the water table in homogeneous and layered soils, *Water*  
960 *Resources Research*, 27, 753-762, 1991.
- 961 Swenson, S. C. and Lawrence, D. M.: Assessing a dry surface layer-based soil resistance  
962 parameterization for the Community Land Model using GRACE and FLUXNET-MTE  
963 data, *Journal of Geophysical Research: Atmospheres*, 119, 10,299-210,312, 2014.
- 964 Swenson, S. C., Lawrence, D. M., and Lee, H.: Improved simulation of the terrestrial  
965 hydrological cycle in permafrost regions by the Community Land Model, *Journal of*  
966 *Advances in Modeling Earth Systems*, 4, n/a-n/a, 2012.
- 967 Tanaka, M., Girard, G., Davis, R., Peuto, A., and Bignell, N.: Recommended table for the  
968 density of water between 0 °C and 40 °C based on recent experimental reports,  
969 *Metrologia*, 38, 301, 2001.
- 970 Taylor, K. E., Stouffer, R. J., and Meehl, G. A.: An Overview of CMIP5 and the Experiment  
971 Design, *Bulletin of the American Meteorological Society*, 93, 485-498, 2012.

972 Taylor, R. G., Scanlon, B., Döll, P., Rodell, M., Van Beek, R., Wada, Y., Longuevergne, L.,  
973 Leblanc, M., Famiglietti, J. S., and Edmunds, M.: Ground water and climate change,  
974 Nature Climate Change, 3, 322-329, 2013.

975 Tian, W., Li, X., Cheng, G. D., Wang, X. S., and Hu, B. X.: Coupling a groundwater model  
976 with a land surface model to improve water and energy cycle simulation, Hydrol.  
977 Earth Syst. Sci., 16, 4707-4723, 2012.

978 van Genuchten, M. T.: A Closed-form Equation for Predicting the Hydraulic  
979 Conductivity of Unsaturated Soils<sup>1</sup>, Soil Science Society of America Journal, 44, 892-  
980 898, 1980.

981 Walko, R. L., Band, L. E., Baron, J., Kittel, T. G. F., Lammers, R., Lee, T. J., Ojima, D., Sr., R.  
982 A. P., Taylor, C., Tague, C., Tremback, C. J., and Vidale, P. L.: Coupled Atmosphere-  
983 Biophysics-Hydrology Models for Environmental Modeling, Journal of Applied  
984 Meteorology, 39, 931-944, 2000.

985 White, M. and STOMP, O. M.: Subsurface transport over multiple phases; Version 2.0;  
986 Theory Guide, Pacific Northwest National Laboratory, 2000. 2000.

987 Yeh, P. J.-F. and Eltahan, E. A. B.: Representation of Water Table Dynamics in a Land  
988 Surface Scheme. Part I: Model Development, Journal of Climate, 18, 1861-1880, 2005.

989 York, J. P., Person, M., Gutowski, W. J., and Winter, T. C.: Putting aquifers into  
990 atmospheric simulation models: an example from the Mill Creek Watershed,  
991 northeastern Kansas, Advances in Water Resources, 25, 221-238, 2002.

992 Yuan, X., Xie, Z., Zheng, J., Tian, X., and Yang, Z.: Effects of water table dynamics on  
993 regional climate: A case study over east Asian monsoon area, Journal of Geophysical  
994 Research: Atmospheres, 113, n/a-n/a, 2008.

995 Zektser, I. S. and Everitt, L. G.: Groundwater resources of the world and their use,  
996 United Nations Educational, Scientific and Cultural Organization<sup>7</sup>, place de Fontenoy,  
997 75352 Paris 07 SP, 2004.

998 Zeng, X. and Decker, M.: Improving the Numerical Solution of Soil Moisture-Based  
999 Richards Equation for Land Models with a Deep or Shallow Water Table, Journal of  
1000 Hydrometeorology, 10, 308-319, 2009.

1001 Zhu, Q., Riley, W. J., Tang, J., and Koven, C. D.: Multiple soil nutrient competition  
1002 between plants, microbes, and mineral surfaces: model development,  
1003 parameterization, and example applications in several tropical forests,  
1004 Biogeosciences, 13, 341-363, 2016.

1005

1006